pISSN: 0256-1115 eISSN: 1975-7220

Nanocomposites of Fe₂O₃@rGO for adsorptive removal of arsanilic acid from aqueous solution

Li-Li Sui*,†, Li-Na Peng**, and Hong-Bo Xu**,†

*Department of Chemistry, Shenyang Medical College, Shenyang 110034, China
**College of Chemical Engineering, University of Science and Technology Liaoning, Anshan, 114051, China
(Received 6 June 2020 • Revised 23 November 2020 • Accepted 24 November 2020)

Abstract–Arsanilic acid (ASA), an organic-arsenic veterinary drug used widely, has greatly attracted attention due to its potential threats. We report the nanocomposites of the α -Fe₂O₃ nanoparticles growth on reduced graphene oxide (rGO) by a one-pot method. The α -Fe₂O₃ nanoparticles are densely covered on the surface of rGO according to the observations of transmission and scanning electron microscope. The adsorptive capacity (357.4±11.2 mg g⁻¹) of the Fe₂O₃@rGO nanocomposites for ASA, which was more than the sum of adsorptive capacities of the pure α -Fe₂O₃ nanoparticles and rGO, revealed a remarkable enhancement due to the synergetic effect of multiple interactions and the good dispersion of α -Fe₂O₃ nanoparticles with more active binding sites in the Fe₂O₃@rGO nanocomposites. The adsorption equilibrium of ASA onto the Fe₂O₃@rGO nanocomposites was achieved for 60 min, and the adsorption of ASA was dependent of pH and temperature, and independent of the concentration of humic acid ranging from 0 to 20 mg L⁻¹. After five cycles of adsorption-desorption, the adsorptive amounts of ASA by the regenerative sorbent still retained 85% of adsorptive amount by the fresh sorbents. The adsorption process of ASA can be described by the Langmuir and the pseudo-second-order equations and is exothermic and spontaneous according to thermodynamic analysis.

Keywords: Arsanilic Acid, Nanocomposites, Graphene, Iron Oxide

INTRODUCTION

Arsanilic acid (4-aminphenylarsonic acid), an organic-arsenic veterinary drug, has been widely employed to promote growth rate, improve feed efficiency and control parasitic diseases for decades in animal-feeding productions [1]. Although the toxicity of arsanilic acid (ASA) is low, the most ingested ASA can be finally excreted in their original form via animal manure and transformed into high toxic inorganic arsenic derivatives under high-moisture and high-temperature conditions during composting [2,3]. The untreated livestock and poultry breeding wastewater enter the soil environment in agriculture, resulting in potential health and environmental risks [4]. Therefore, the effective removal of ASA from the culture wastewater is a crucial requirement for controlling arsenic contamination.

The concentration of ASA in the breeding wastewater is at the level of mg L⁻¹ [5]. For the removal of the low-level ASA from the culture wastewater, adsorption is the preeminent method and especially suitable for the treatment of wastewater containing low-concentration pollutants. Some sorbents have been developed for the removal of the organic-arsenic compounds, including metal-organic framework [6], metallic oxide [7], iron (oxyhydr)oxides [8], magnetic greigite [9], molecularly imprinted polymers [10], mineral [11], chitosan [12] and carbon nanotubes [13]. Recently, nanocomposites have exhibited superior performance for the adsorption of organic-arsenic compounds [14-17]. Kong and Wilson [14] reported a binary

goethite-cellulose nanocomposite with the advantage of enhanced adsorption of organic-arsenic compound due to the good dispersion of goethite nanoparticles (NPs). Hu et al. [15] developed Femodified carbon nanotubes which have higher adsorption capacity of organic-arsenic compound than the unmodified carbon nanotubes due to synergetic effect of multiple interactions. The binary nanocomposites of Fe₃O₄ NPs and reduced graphene oxide (rGO) were developed for the removal of organic-arsenic compounds with higher adsorption capacity compared to the pure Fe₃O₄ NPs and rGO because of the multiple interactions [16,17]. The rGO as the dispersion support of NPs exhibited the highest adsorption capacity of the organic-arsenic compounds because the planar geometry of rGO is amenable modification or functionalization, providing the fabricated adsorbents with the desired properties [18]. Chen and co-workers found that Fe³⁺, Zn²⁺ and Cu²⁺ dramatically enhanced the adsorption of organic-arsenic compounds on goethite surface [19]. Compared with other metals, Fe³⁺ is a common and cheap element. The α -Fe₂O₃ NPs have been confirmed to be alternative sorbents for the removal of arsenic through the surface As-Fe coordination [20]. Due to the agglomeration of α -Fe₂O₃ NPs, the surface complexation of α -Fe₂O₃ NPs with ASA was weakened. The nanocomposites of the well-dispersed α -Fe₂O₃ NPs on the rGO combine the advantages of α-Fe₂O₃ NPs and rGO, which could improve the adsorptive properties of ASA [21].

In this work, the nanocomposites of Fe_2O_3 @rGO were developed and prepared via *in-situ* crystal growth of Fe_2O_3 NPs onto the surface of rGO with hydrothermal process. The objective of this work is to assess the adsorptive process of ASA by the Fe_2O_3 @rGO and their possible mechanisms, which would provide an understanding of the role of the Fe_2O_3 @rGO for the treatment of ASA

[†]To whom correspondence should be addressed. E-mail: sllsqy123@126.com, lnkdxhb@163.com Copyright by The Korean Institute of Chemical Engineers. in the contaminated wastewater.

EXPERIMENTAL

1. Preparation and Characterization of the $Fe_2O_3@rGO$ Nano-composite

Graphene oxide (GO) was obtained as described in Supporting Information [22]. The product was obtained by centrifugation (16,000 rpm) for 5 min and washing with deionized water to no presence of sulfate ions. Finally, the as-synthesized GO powder was dried at 60 °C for constant weight.

0.40~g of $FeCl_3 \cdot 9H_2O$ was dissolved in 50~mL of ethanol and then the $FeCl_3$ ethanol solution was mixed into 100~mL of the GO suspension aqueous solution ($1~g~L^{-1}$) under magnetic stirring for 15~min. NH_3 solution (30~mL) was mixed dropwise. After the hydrothermal reaction of the mixture at $180~^{\circ}C$ for 48~h, the obtained products were isolated by centrifugation (16,000~rpm) for 10~min, washed with methanol, and dried in vacuum at $60~^{\circ}C$ overnight. For comparison, the $Fe_2O_3~NPs$, and the rGO were also prepared using the identical procedure as above. All the reagents and apparatus used are also listed in Supporting Information. The characterization methods are described in Supporting Information.

2. Batch Experiments

The adsorption of ASA on the Fe₂O₃@rGO was tested using batch method. Effect of Fe₂O₃@rGO dosage (1-8 g L⁻¹) on the removal efficiency was tested in ASA solution (20 mL) with 100 mg L⁻¹ at pH 5 for 120 min. The ASA solution (20 mL) with varying concentration (100-700 mg L⁻¹) by adding a fixed dose of Fe₂O₃@rGO was stirred for a specified period at desired pH and temperature with stirring rate of 200 rpm. The dosage of the Fe₂O₃@rGO was kept at $4\,\mathrm{g}\,\mathrm{L}^{-1}$. Temperature was adapted to 25, 35 and 45 °C to test the influence of temperature. To measure the influence of contact time on adsorption amounts, the contact time was varied from 10 to 120 min. Influence of pH (3-10) on the removal of ASA was tested at 25 °C for 60 min through modulating solution pH using HCl or NaOH solutions. The typically content of dissolved natural organic matter (DNOM) was below 20 mg L⁻¹ in water [23]. The effect of DNOM as humic acid (HA) on the removal efficiency was tested in a solution containing ASA of 100 mg L⁻¹ and DNOM of 0, 5, 10, 20 mg L⁻¹. The pH of solution was controlled at pH 9 because HA is water-soluble in alkaline solution. The reuse of the Fe₂O₃@rGO was tested in five cycles of adsorption-desorption using acidic ethanol acidified with 0.1 mol L-1 HCl at pH 3 as the eluent according to the previous method [6]. The loaded Fe₂O₃@rGO was added in acidic ethanol with stirring for 6h, and then the regenerative sorbents were filtrated, washed with deionized water near neutral and dried for the next cycle. All the trials were performed in triplicate and all the measurement data were expressed as the average± standard deviation (SD) at the 5% significance level. After stable situation, the concentration of the ASA in the remnant solution was estimated by a high-performance liquid chromatography (HPLC) method [24]. The adsorptive amount was obtained by Eq. (1) as follows.

$$q = (C_0 - C_t) V/m \tag{1}$$

where q (mg g^{-1}) is the adsorption capacity, C_0 (mg L^{-1}) is the ini-

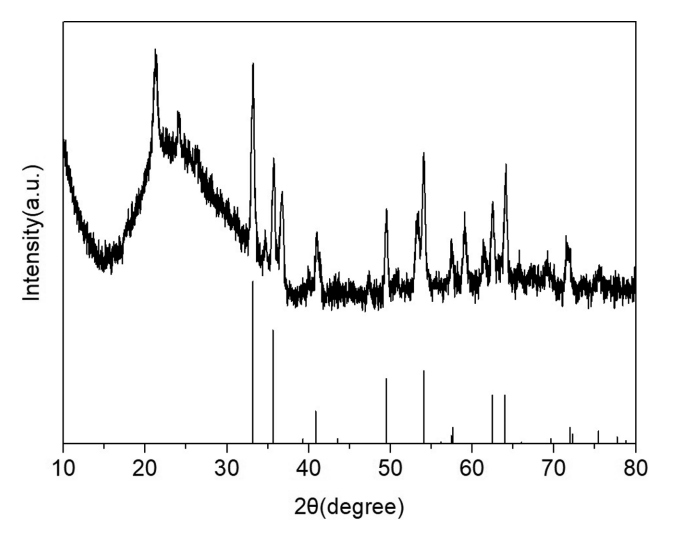


Fig. 1. XRD patterns of the Fe₂O₃@rGO.

tial concentration of ASA, C_t (mg L^{-1}) is the remnant concentration of ASA, V (mL) is the volume of solution and m (g) is the mass of Fe₂O₃@rGO nanocomposite.

RESULTS AND DISCUSSION

1. Characterization

From Fig. 1, the strong and sharp XRD peaks for the crystal phase of well-crystallized Fe₂O₃ NPs are consistent with the peaks of α -Fe₂O₃ particles (JCPDS No. 33-0664) [25], illustrating that the α -Fe₂O₃ particles have been introduced into the hybrid sorbent. Lack of XRD peaks of rGO at 26° is detected due to the overlap of the large amounts of α -Fe₂O₃ particles onto the rGO surface [26].

The 1-D rod-like Fe₂O₃ NPs are formed in the width range of 20-50 nm (Fig. S1(a)) and the well-packed layers of RGO sheets are observed in Fig. S1(b). Large amount coverage of rod-like Fe₂O₃ NPs anchored uniformly on both sides of the rGO sheets can be observed in Fig. 2(a), suggesting the rGO sheets as the stable support for anchoring 1-D Fe₂O₃ NPs. Fe₂O₃ NPs are randomly and well dispersed on the rGO sheets, indicating an efficient assembly between the Fe₂O₃ NPs and rGO sheets during the hydrothermal process. From Fig. 2(b), the SEM image of the Fe₂O₃@rGO agrees with its TEM image and the rod-like Fe₂O₃ NPs are anchored fully on the rGO surface. The presence of a large amount of Fe element in the Fe₂O₃@rGO from the EDS results can confirm the growth of Fe₂O₃ NPs on the rGO surface. The Fe₂O₃@rGO displays the BET surface area of 163 m² g⁻¹ and pore volume of 0.306 cm³ g⁻¹. The average pore diameter is estimated to be 0.548 nm. From Fig. 3, the characteristics of Fourier transmission infrared spectrum (such as a band of Fe-O bonds at 571 cm⁻¹, the aromatic C=C stretching vibration at 1,550 cm⁻¹, a shoulder band of the bridging coordinated carboxylates at 1,625 cm⁻¹ and a band of carboxyl group at 1,742 cm⁻¹) reveal the presence of Fe₂O₃ and rGO in the Fe₂O₃@rGO [27]. The surface element distribution of the Fe₂O₃@rGO was analyzed by XPS spectrum (Fig. S1). The two peaks at 710.8 and 724.4 eV are assigned to the transitions of Fe 2p3/2 and Fe 2p1/2, which is consistent with hematite phase [28].

500 L.-L. Sui et al.

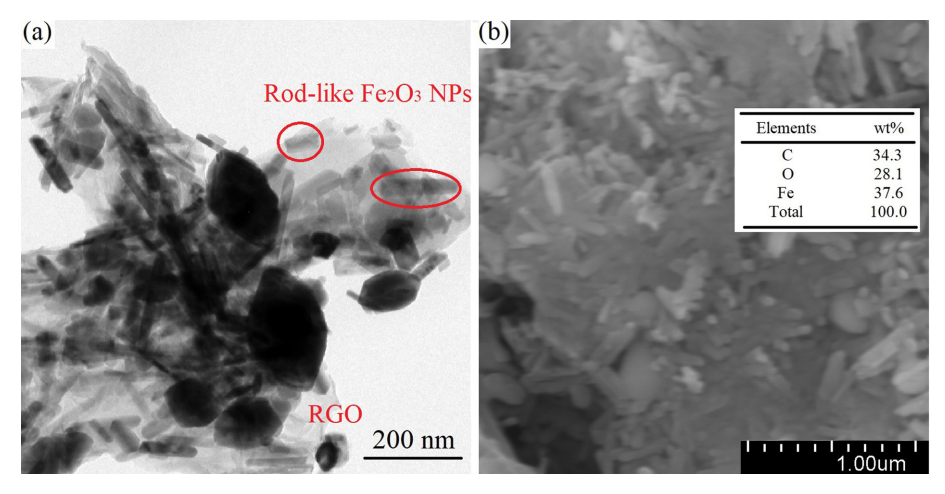


Fig. 2. (a) TEM and (b) SEM images of the Fe₂O₃@rGO.

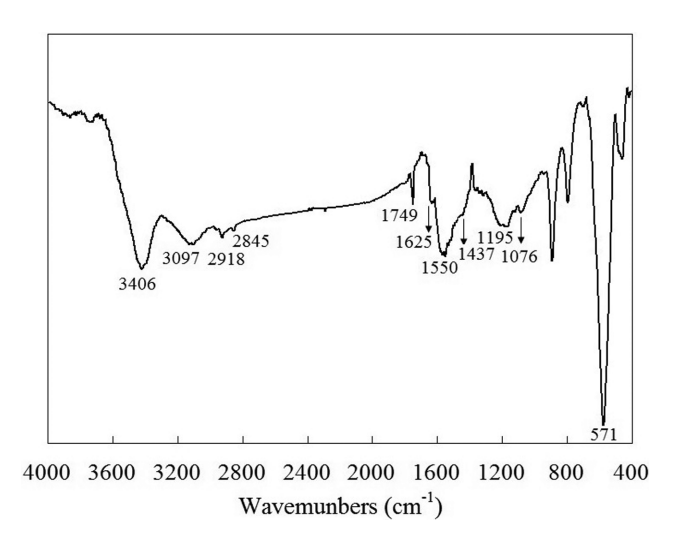


Fig. 3. Fourier transmission infrared spectrum of the Fe₂O₃@rGO.

2. Effect of Fe₂O₃@rGO Dosage

The removal efficiency of ASA in solution increased from 42.4% to 97.2% with the increase in the Fe $_2$ O $_3$ @rGO dosage in the range of 1-4 g L $^{-1}$ (Fig. S2). There was no obvious difference of removal efficiency in the Fe $_2$ O $_3$ @rGO dosage from 5 to 8 g L $^{-1}$. These results indicate that the Fe $_2$ O $_3$ @rGO dosage of 4 g L $^{-1}$ was sufficient.

3. Effect of Contact Time

The adsorption of ASA by the Fe_2O_3 @rGO took place very quickly within the first 30 min (Fig. 4) due to a large amount of available binding sites in the Fe_2O_3 @rGO and a large concentration gradient on the interface of solid-liquid at the beginning, and hence the transfer of ASA onto the surface of the Fe_2O_3 @rGO was faster. Within the second 30 min, the uptake was slowed because ASA took more time to transport from the surface to internal binding sites. After 60 min, the uptake was settled off and changed insignificantly, indicating that a state of equilibrium was reached. As time increased, the binding sites on the surface of the Fe_2O_3 @rGO became exhausted. Our findings were also reported by other researchers, such as a quick uptake of roxarsone in the initial stage by the carbon nanotubes [13] and by the metal-organic frameworks [29].

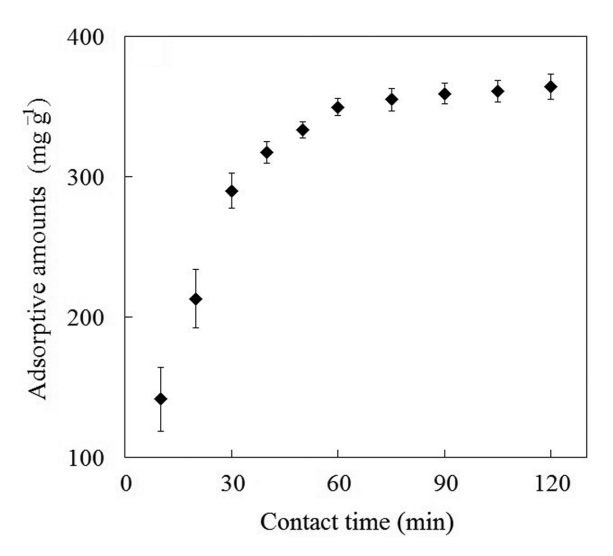


Fig. 4. Effect of contact time.

Therefore, 60 min was suitable as the contact time of ASA adsorption for the subsequent trials.

4. Effect of pH

ASA contains benzene ring, amino group and one arsenic ion with the aqueous dissociation constants (p K_{a1} =1.9 p K_{a2} =4.1 and pK_{a3} =9.2) [7] and there exists the various chemical speciation in the variation of solution pH. The point of zero charge of pH (pH_{PZC}) for the Fe₂O₃@rGO was obtained as in the previous method [30]. The pH_{PZC} of the Fe₂O₃@rGO was 6.7±0.4 according to the pH drift method [30], suggesting that the surface of the Fe₂O₃@rGO was cationic below pH_{PZC} and anionic above pH_{PZC} . The pH-dependence of ASA adsorption is observed as illustrated in Fig. 5. It was found that there was no notable change in the adsorptive amount of ASA by the Fe₂O₃@rGO in the range of pH 3-6 because there was an electrostatic interaction between the negatively charged ASA and the cationic surface of the Fe₂O₃@rGO as the dominant interaction forces. In pH ranging from 6 to 10, the adsorptive amount of ASA by the Fe₂O₃@rGO obviously reduced because of the electrostatic repulsion of the same charged ASA and Fe₂O₃@rGO

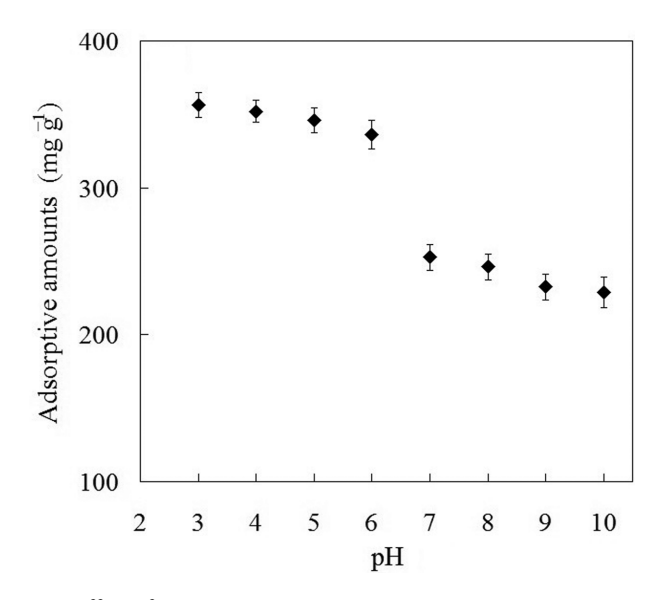


Fig. 5. Effect of pH.

[31]. Another factor might be that the dissociated species of ASA at high pH inhibited the formation of hydrogen bonds with rGO [15]. These made an unfavorable adsorption of ASA by the Fe₂O₃@rGO at pH>6. However, about 65% of adsorptive amount of ASA at pH≤6 was observed in the pH range of 6-10, illustrating that the in the adsorption of ASA existed other interactions such as (As-Fe coordination) other than electrostatic interactions and/or hydrogen bonds [8,32]. Adamescu and co-workers calculated the binding energy of the As-Fe coordination up to 20 kcal mol⁻¹ [33]. Tian and co-workers found that the contribution of the interactions to the adsorption of the organic-arsenic compounds was in the order: As-Fe coordination>hydrogen bonding> π - π interaction [16]. Therefore, the Fe₂O₃@rGO still kept a relatively high adsorptive amount at pH>6 due to the stable interaction of As-Fe coordination. Similar results had been exhibited by other research [6,34]. Therefore, the pH of 5 was used as the desired pH for the ASA adsorption in the subsequent trials.

5. Adsorbed Amounts

As the initial concentration enhanced, the adsorptive amount of ASA by the Fe_2O_3 NPs, the pure rGO and the Fe_2O_3 @rGO increased (Fig. 6). The Fe_2O_3 @rGO was used as an example, and the adsorptive amount of ASA was dependent on the ASA concentrations from 100 to 500 mg L^{-1} in feed solution. After 500 mg L^{-1} , a small

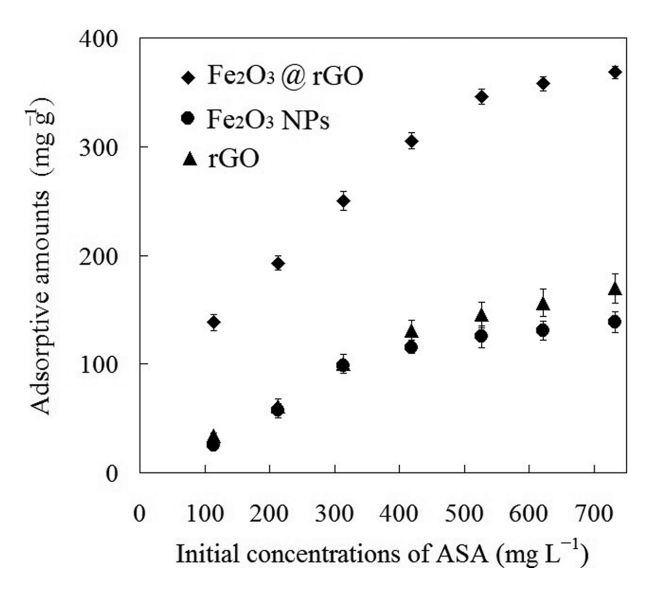


Fig. 6. Effect of the initial ASA concentration.

variation in the adsorptive amount of ASA by the Fe₂O₃@rGO was exhibited. The experimental values of the adsorptive amount of ASA by the Fe₂O₃ NPs, the rGO and the Fe₂O₃@rGO were found to be 127.5 ± 6.7 , 150.5 ± 12.3 and 357.4 ± 11.2 mg g⁻¹, respectively. The adsorptive amount of ASA by the Fe₂O₃@rGO was more than the sum of adsorptive amounts of the Fe₂O₃ NPs and the rGO. This phenomenon is attributed to (1) the synergetic effect of multiple interactions of Fe₂O₃@rGO with ASA (such as electrostatic force, hydrogen bonding, As-Fe coordination and π - π interaction) [16], (2) the good dispersion of Fe₂O₃ NPs on the rGO in the hybrid process which is a benefit for the formation of As-Fe surface coordination [35,36], and (3) the formation of more active binding sites of the Fe₂O₃@rGO. These factors led to a notable increase in the adsorption amount of ASA by the Fe₂O₃@rGO compared with the Fe₂O₃ NPs and the rGO. Similar phenomena were also described for other nanocomposites [16,17]. There was a comparison of the Fe₂O₃@rGO nanocomposites in the adsorptive amount of ASA with previously reported sorbents as listed in Table 1 [6,8,17,32,36-38]. The Fe₂O₃@rGO nanocomposites has relatively high adsorptive amounts and relatively rapid adsorptive rate compared with most of previously reported sorbents. Fig. S3 displays that the presence of HA has no significant matrix effect. Inhibition influence on the removal efficiency of ASA was not ob-

Table 1. Comparison of various sorbents toward ASA adsorption

	*		
Sorbents	Capacity (mg g ⁻¹)	Contact time	Ref.
Zeolitic imidazolate framework-8	791.1	6 h	[6]
Iron (oxyhydr) oxides	156.3	5 h	[8]
Fe ₃ O ₄ @RGO	313.7	15 min	[17]
Metal-organic frameworks	302.3	3 h	[31]
Goethite	213.6	5 h	[35]
Iron humate	188.7	5 h	[36]
MgO	86.8	7 h	[37]
Fe ₂ O ₃ @RGO	357.4	60 min	This work

502 L.-L. Sui et al.

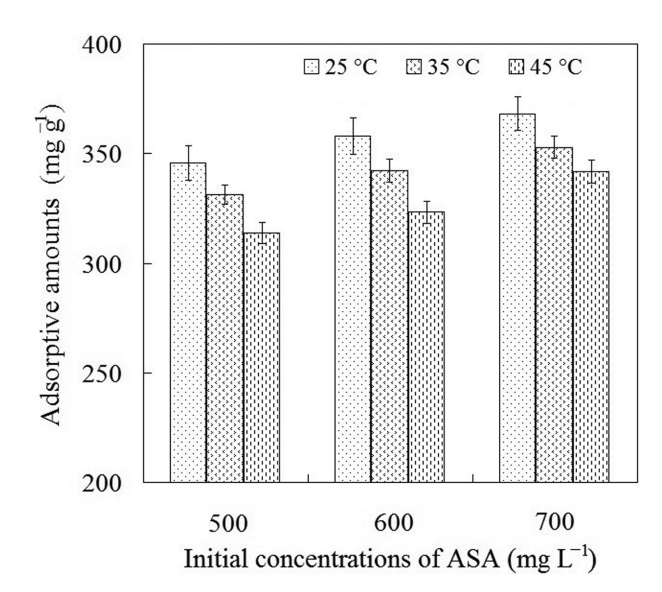


Fig. 7. Effect of temperature.

Table 2. Isotherms parameters for the adsorption of ASA at 25 °C

Langmuir	Freundlich	D-R
q_{max} =423.7 mg g ⁻¹	$K_F = 19.81 \text{ L g}^{-1}$	k_{ad} =0.0049 mol ² kJ ⁻²
b=0.01145 L mg ⁻¹	1/n=0.471	$q_s = 1,517.8 \text{ mg g}^{-1}$ E=10.1 mol kJ ⁻¹
$R^2 = 0.9991$	$R^2 = 0.9866$	$R^2 = 0.9921$

served as the HA concentration ranged from 0 to 20 mg L^{-1} . Due to the formation of firm bond via surface coordination of ASA with the Fe₂O₃@rGO, ASA was not suffering the competitive adsorption with HA on the surface of Fe₂O₃@rGO.

6. Effect of Temperature

The adsorptive amount of ASA by the Fe₂O₃@rGO decreased slightly with the increase of temperature 25-45 °C (Fig. 7), indicating that the adsorption of ASA was exothermic and a higher temperature was unfavorable for the adsorption of ASA. The exothermic characteristics of the Fe₂O₃@rGO for the ASA adsorption could be attributed to the fact that the complexation of As-Fe and the π - π interaction between rGO and ASA were exothermic reactions [13,33]. Similar trends were found by the previous reports [15,16].

7. Adsorption Isotherm

The equilibrium data were further fitted with three adsorption isotherms: Langmuir, Freundlich and Dubinin-Radushkevich (D-R) [39,40]. The fitting equations of these isotherms are described in Supporting Information. From Table 2 and Fig. S5, the R² values from Langmuir (0.9991) and D-R (0.9921) models are higher than that from Freundlich (0.9866) model, illustrating that the ASA

Table 4. Thermodynamic parameters for adsorption of ASA

Thermodynamic	Temperature (°C)		
constants	25	35	45
lnb	9.35	9.19	9.14
ΔG^{o} (kJ mol ⁻¹)	-23.16	-23.54	-24.15
ΔH^o (kJ mol ⁻¹)	-8.38		
ΔS^{o} (J mol ⁻¹ K ⁻¹)	49.47		

adsorption maybe follows the Langmuir and D-R models. Moreover, the theoretical maximum adsorption amount of ASA from Langmuir model was found to be 423.7 mg g $^{-1}$ and closer to the experimental value than the theoretical value from D-R model of 1,517.8 mg g $^{-1}$, illustrating that Langmuir model is more suitable to reflect the feature of the ASA adsorption on the Fe₂O₃@rGO with a higher reliability. The E value from D-R model was calculated to be 10.1 mol k Γ^{-1} , which follows the energetic range of chemical adsorption [41], illustrating that the chemical interaction between ASA and the Fe₂O₃@rGO may occur during the adsorptive process [42]. In brief, the Langmuir model provides a more representative description for the ASA adsorption by the Fe₂O₃@rGO.

8. Kinetic Study

The data were also fitted with three kinetic models (such as pseudo-first-order (PFO), pseudo-second-order (PSO) and Elovich models) [43]. The fitting kinetic equations are described in Supporting Information. According to Table 3 and Fig. S6, the R^2 values from PFO and Elovich equations were found to be 0.9626 and 0.9176, respectively, which were lower than that obtained from the PSO equation (0.9948), demonstrating that the PFO and Elovich plots were not satisfactory for fitting the kinetic data. In addition, the q_{eq} value calculated of ASA from the PSO equation is nearly consistent with the experimental value, while the q_{eq} value calculated of ASA from the PFO equation is significantly lower than its experimental value. Therefore, the PSO model can well represent the kinetic process of ASA adsorption by the Fe₂O₃@rGO.

9. Thermodynamic Study

The thermodynamic parameters were calculated using the equations as listed in Supplementary Material. The standard enthalpy change (ΔH°), the standard entropy change (ΔS°) and the change in standard free energy of Gibbs (ΔG°) were calculated as described previously (as listed in Table 4) [44]. The value of ΔG° at 25, 35 and 45 °C was found to be –19.4, –19.6 and –20.1 kJ mol⁻¹, respectively, confirming the feasibility and spontaneity of the ASA adsorption by the Fe₂O₃@rGO [45]. The negative value of ΔH° (–8.4 kJ mol⁻¹) revealed that the uptake of ASA was exothermic, suggesting that a low temperature in the tested range was more favorable for the adsorption of ASA, which was in accordance with the results obtained from Fig. 3(d). The positive value of ΔS° (36.8 J

Table 3. Calculated kinetic parameters for the adsorption of ASA

Pseudo-first-order	Pseudo-second-order	Elovich
k_1 =0.034 min ⁻¹ q_{eq} (cal)=208.9 mg g ⁻¹ R^2 =0.9626	$k_2=0.18\times10^{-3} \text{ g mg}^{-1} \text{ min}^{-1}$ $q_{eq}(\text{cal})=416.7 \text{ mg g}^{-1}$ $R^2=0.9948$	α =246.5 mg g ⁻¹ min ⁻¹ β =0.023 g ⁻¹ mg R ² =0.9176

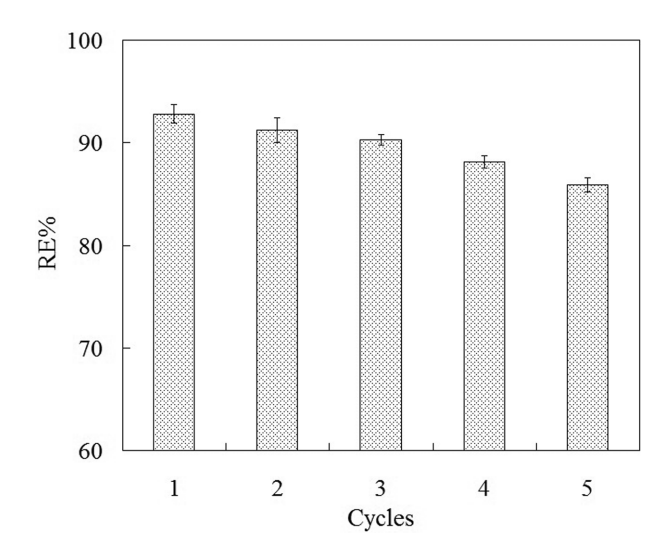


Fig. 8. Reusability of the regenerated Fe₂O₃@RGO.

 $\text{mol}^{-1} \text{ K}^{-1}$) suggested the increase of randomness, which might be attributed to the desorption of several molecules of solvent as each molecule of ASA adsorbed [46]. Similar results were also observed in previous literature [6,47].

10. Reusability

Five cycles of the adsorption-desorption were carried out to test the reusability of the $Fe_2O_3@rGO$ (Fig. 8). The regenerative efficiency (RE) can be calculated by Eq. (2) as follows:

RE %=
$$(Q_{Regenerated}/Q_{Fresh}) \times 100\%$$
 (2)

where $Q_{Regenerated}$ (mg g^{-1}) is an adsorptive amount of ASA by the regenerative Fe_2O_3 @rGO, and Q_{Fresh} (mg g^{-1}) is an adsorptive amount of ASA by the fresh Fe_2O_3 @rGO. The values of ER% decreased slightly with the increase of in cycle numbers. The adsorptive amounts of ASA by the regenerative Fe_2O_3 @rGO were close to 85% of the fresh Fe_2O_3 @rGO, indicating that the Fe_2O_3 @rGO was a reusable sorbent and could be recycled. The concentration of Fe ions in the eluent was not detected by flame atomic absorption spectrometry, indicating that there was no notable Fe leach from the Fe_2O_3 @rGO during the process of elution.

CONCLUSION

A nanocomposite of the Fe_2O_3 @rGO with the good performance of the ASA adsorption was prepared. The Fe_2O_3 @rGO nanocomposites had better-adsorbed amounts, faster-adsorbed rate and good reusability. The higher adsorptive amount of ASA by the Fe_2O_3 @rGO was observed in the range of pH 3-6. The adsorption amount of ASA by the Fe_2O_3 @rGO was improved significantly due to the synergetic effect of multiple interactions, the good dispersion of Fe_2O_3 NPs on the surface of rGO and the formation of more active binding sites. There was no significant inhibition influence of HA on the removal efficiency of ASA in the range of HA from 0 to 20 mg L^{-1} . A decrease in the adsorptive amount of ASA by the Fe_2O_3 @rGO was found with the increase in temperature during 25-45 °C due to its exothermicity. The ASA adsorption followed well the Langmuir and PSO models and was a spontaneous process.

ACKNOWLEDGEMENTS

Financial support of this work was provided by the Science and technology development fund of Shenyang Medical College (20191026) and by scientific research foundation of education department of Liaoning province (LN201902).

SUPPORTING INFORMATION

Additional information as noted in the text. This information is available via the Internet at http://www.springer.com/chemistry/journal/11814.

REFERENCES

- 1. L. R. Overby and S. Lilian, Toxicol. Appl. Pharmacol., 7, 850 (1965).
- 2. D. W. Rutherford, A. J. Bednar, J. R. Garbarino, R. Needham, K. W. Staver and R. L. Wershaw, *Environ. Sci. Technol.*, **37**, 1515 (2003).
- 3. J. R. Garbarino, A. J. Bednar, D. W. Rutherford, R. S. Beyer and R. L. Wershaw, *Environ. Sci. Technol.*, **37**, 1509 (2003).
- B. L. Brown, A. D. Slaughter and M. Schreiber, Appl. Geochem., 20, 123 (2005).
- J. Xu, X. Shen, D. Wang, C. Zhao, Z. Liu, I. P. Pozdnyakov, F. Wu and J. Xia, *Chem. Eng. J.*, 336, 334 (2018).
- B. K. Jung, J. W. Jun, Z. Hasan and S. H. Jhung, Chem. Eng. J., 267, 9 (2015).
- 7. S. Chen, J. Deng, C. Ye, C. Xu, L. Huai, J. Li and X. Li, *Sci. Total Environ.*, **742**, 140587 (2020).
- T. P. Joshi, G. Zhang, R. Koju, Z. Qi, R. Liu, H. Liu and J. Qu, Sci. Total Environ., 601-602, 713 (2017).
- 9. W. Liu, Z. Ai, R. A. Dahlgren, L. Zhang and X. Wang, *Chem. Eng. J.*, **330**, 1232 (2017).
- W. Fan, X. Zhang, Y. Zhang, P. Wang, L. Zhang, Z. Yin, J. Yao and W. Xiang, J. Mol. Recognit., 31, e2625 (2018).
- 11. Y.-J. Wang, F. Ji, W. Wang, S.-J. Yuan and Z.-H. Hu, *Desalin. Water Treatm.*, **57**, 20520 (2016).
- L. Poon, S. Younus and L. D. Wilson, J. Colloid Interface Sci., 420, 136 (2014).
- 13. J. Hu, Z. Tong, Z. Hu, G. Chen and T. Chen, *J. Colloid Interface Sci.*, **377**, 355 (2012).
- 14. D. Kong and L. D. Wilson, Carbohyd. Polym., 169, 282 (2017).
- 15. J. Hu, Z. Tong, G. Chen, X. Zhan and Z. Hu, *Int. J. Environ. Sci. Technol.*, **11**, 785 (2014).
- C. Tian, J. Zhao, J. Zhang, S. Chu, Z. Dang, Z. Lin and B. Xing, Environ. Sci.: Nano, 4, 2134 (2017).
- N. You, X.-F. Wang, J.-Y. Li, H.-T. Fan and Q. Zhang, J. Ind. Eng. Chem., 70, 346 (2019).
- 18. T. A. Saleh, M. M. Al-Shalalfeh and A. A. Al-Saadi, *Sensors Actuat. B: Chem.*, **254**, 1110 (2018).
- 19. L. Y. Wang, S. W. Wang and W. R. Chen, *Chemosphere*, **152**, 423 (2016).
- 20. W. Tang, Q. Li, S. Gao and J. K. Shang, *J. Hazard. Mater.*, **192**, 131 (2011).
- 21. X. Zhao, L. Lv, B. Pan, W. Zhang, S. Zhang and Q. Zhang, *Chem. Eng. J.*, **170**, 381 (2011).
- 22. W.S. Hummers and R.E. Offeman, J. Am. Chem. Soc., 80, 1339

504 L.-L. Sui et al.

(1958).

- 23. N. You, Y. Chen, Q.-X. Zhang, Y. Zhang, Z. Meng and H.-T. Fan, *Sci. Total Environ.*, 735, 139553 (2020).
- 24. F.-F. Zhang, W. Wang, S.-J. Yuan and Z.-H. Hu, J. Hazard. Mater., 279, 562 (2014).
- 25. M. Sun, H. Liu, Y. Liu, J. Qu and J. Li, Nanoscale, 7, 1250 (2015).
- K. Urbas, M. Aleksandrzak, M. Jedrzejczak, M. Jedrzejczak, R. Rakoczy, X. Chen and E. Mijowska, *Nanoscale Res. Lett.*, 9, 656 (2014).
- 27. C. Z. Zhu, S. J. Guo, Y. X. Fang and S. J. Dong, *ACS Nano*, **4**, 2429 (2010).
- 28. C. Wu, H. Zhang, Y. X. Wu, Q. C. Zhuang, L. L. Tian and X. X. Zhang, *Electrochim. Acta*, **134**, 18 (2014).
- B. Li, X. Zhu, K. Hu, Y. Li, J. Feng, J. Shi and J. Gu, J. Hazard. Mater., 302, 57 (2016).
- 30. I. I. Salame and T. J. Bandosz, J. Colloid Interface Sci., 240, 252 (2001).
- 31. J. Deng, Y.-J. Chen, Y.-A. Lu, X.-Y. Ma, S.-F. Feng, N. Gao and J. Li, *Environ. Sci. Pollut. Res.*, **24**, 14396 (2017).
- 32. J. W. Jun, M. Tong, B. K. Jung, Z. Hasan, C. Zhong and S. H. Jhung, *Chem. Eur. J.*, **21**, 347 (2015).
- 33. A. Adamescu, I. P. Hamilton and H. A. Al-Abadleh, *J. Phys. Chem. A*, **118**, 5667 (2014).
- 34. T. Sun, Z. Zhao, Z. Liang, J. Liu, W. Shi and F. Cui, *Chem. Eng. J.*, 334, 1527 (2018).
- 35. W. Mitchell, S. Goldberg and H. A. Al-Abadleh, J. Colloid Interface

- Sci., 358, 534 (2011).
- 36. W. R. Chen and C. H. Huang, J. Hazard. Mater., 227-228, 378 (2012).
- 37. Y. Peng, W. Wei, H. Zhou, S. Ge, S. Li, G. Wang and Y. Zhang, *J. Dispers. Sci. Technol.*, 37, 1590 (2016).
- 38. T. P. Joshi, G. Zhang, H. Cheng, R. Liu, H. Liu and J. Qu, *Water Res.*, **116**, 126 (2017).
- 39. H.-T. Fan, J.-B. Wu, X.-L. Fan, D.-S. Zhang, Z.-J. Su, F. Yan and T. Sun, *Chem. Eng. J.*, **198-199**, 355 (2012).
- 40. H.-T. Fan, X.-T. Sun, Z.-G. Zhang and W.-X. Li, *J. Chem. Eng. Data*, **59**, 2106 (2014).
- 41. H. Javadian, P. Vahedian and M. Toosi, *Appl. Surf. Sci.*, **284**, 13 (2013).
- 42. H.-T. Fan, Q. Tang, Y. Sun, Z.-G. Zhang and W.-X. Li, *Chem. Eng. J.*, **258**, 146 (2014).
- 43. H.-T. Fan, X.-T. Sun and W.-X. Li, J. Sol-Gel Sci. Technol., 72, 144 (2014).
- 44. Y. Liu, J. Chem. Eng. Data, 54, 1981 (2009).
- H.-T. Fan, W. Sun, B. Jiang, Q.-J. Wang, D.-W. Li, C.-C. Huang, K.-J. Wang, Z.-G. Zhang and W.-X. Li, *Chem. Eng. J.*, 286, 128 (2016).
- 46. H. Fan, X. Fan, J. Li, M. Guo, D. Zhang, F. Yan and T. Sun, *Ind. Eng. Chem. Res.*, **51**, 5216 (2012).
- 47. H.-T. Fan, Y. Sun, Q. Tang, W.-L. Li and T. Sun, *J. Taiwan Inst. Chem. Eng.*, **45**, 2640 (2014).

Supporting Information

Nanocomposites of Fe₂O₃@rGO for adsorptive removal of arsanilic acid from aqueous solution

Li-Li Sui*,†, Li-Na Peng**, and Hong-Bo Xu**,†

*Department of Chemistry, Shenyang Medical College, Shenyang 110034, China
**College of Chemical Engineering, University of Science and Technology Liaoning, Anshan, 114051, China
(Received 6 June 2020 • Revised 23 November 2020 • Accepted 24 November 2020)

Materials

Graphite powder was purchased from Qingdao Xiyou Fine Graphite Chemical Co., LTD (Qingdao, China). All the other reagents were at least of analytical grade and obtained from Sinopharm Chemical Reagent Co., Ltd (Shanghai, China).

Characterization

The product obtained was characterized by X-ray diffraction using Cu K\$\alpha\$ radiation (XRD, Almelo PW-3060, Netherland), A Shimadzu SSX-550 scanning electron microscope (SEM) combined with an energy-dispersive X-ray spectroscopy (EDS), and TECNAI G20 transmission electron microscope (TEM, FEI, USA). The absorption spectra of the samples were taken at room temperature by a Nicolet 6700 Fourier transmission infrared spectroscopy (FT-IR) in the range of 400-4,000 cm $^{-1}$ with a resolution of 1 cm $^{-1}$ using KBr window and a BWS465-785S laser confocal Raman spectroscopy (B&W Tek LLC, USA). The chemical environment of the surface composition of the Fe2O3@rGO nanocomposites was recorded by Thermo Scientific ESCALAB 250Xi X-ray photoelectron spectroscopy (XPS, Thermo, Waltham, USA). Textural characterization of the adsorbents was accomplished by N2 adsorption-desorption isotherms at 77 K.

Analysis

The concentrations of ASA were determined by high-performance liquid chromatography (HPLC) at 264 nm with C_{18} column using the mixture solution of 0.05 mol L^{-1} KH₂PO₄ containing 0.1% formic acid (v/v) and methanol in a 95:5 (v/v) ratio with a flow rate of 1.0 mL min⁻¹ at 30 °C.

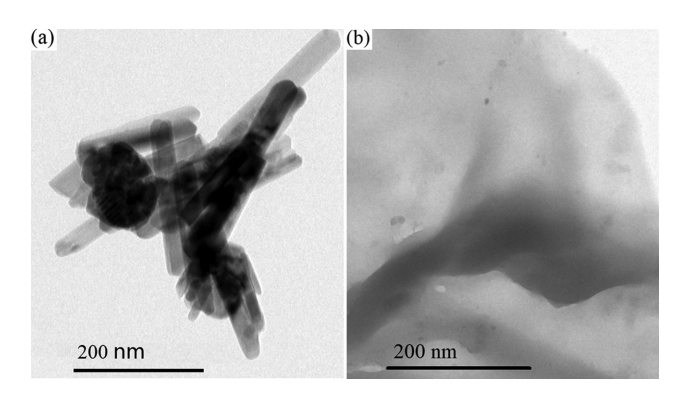


Fig. S1. TEM images of (a) Fe₂O₃ NPs and (b)RGO.

Calculation of adsorption capacity

$$q=(C_0-C_t) V/m$$
 (S1)

where q (mg g^{-1}) is the adsorption capacity, C_0 (mg L^{-1}) is the ini-

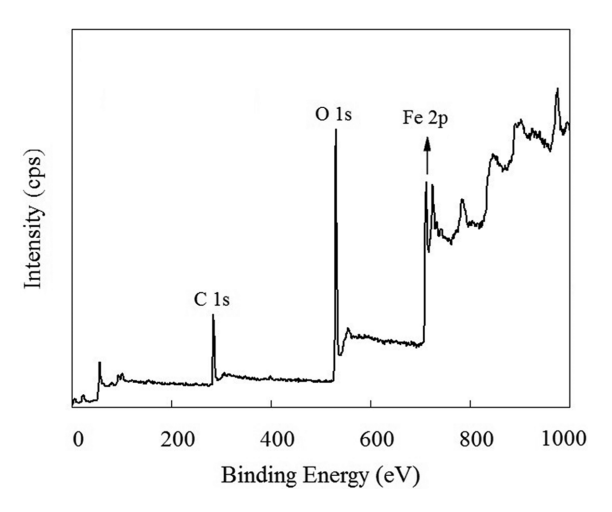


Fig. S2. Wide scan XPS spectrum of the Fe₂O₃@rGO.

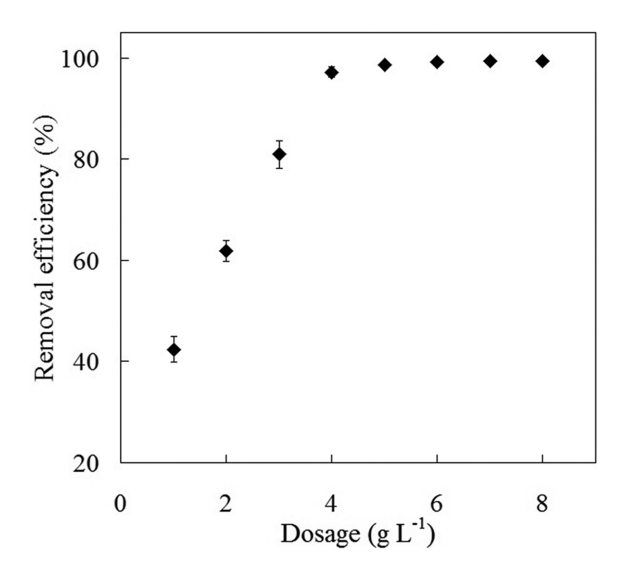


Fig. S3. Effect of dosage.

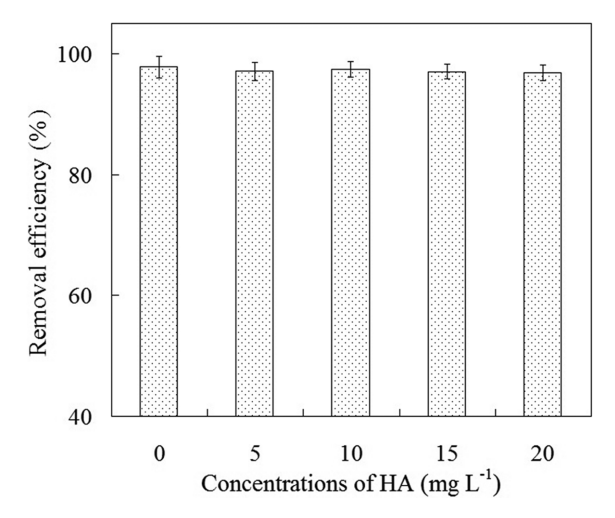


Fig. S4. Effect of HA.

tial concentration of ASA, C_t (mg L^{-1}) is the remnant concentration of ASA, V (mL) is the volume of solution and m (g) is the mass of Fe₂O₃@rGO nanocomposite.

Adsorption isotherms

The linearized equations of Langmuir, Freundlich and Dubinin-

Radushkevich (D-R) isotherm can be expressed as Eqs. (S1) and (S2), respectively.

$$C_e/q_e=1/(q_{max} b)+C_e/q_{max}$$
 (S2)

$$\log q_e = \log k_F + (1/n) \log C_e \tag{S3}$$

$$\ln q_e = \ln q_s - k_{ad} \varepsilon^2 \tag{S4}$$

where q_{ϵ} (mg g^{-1}) is the amount of Ca^{2+} ions adsorbed per unit mass of BCES at equilibrium; C_{ϵ} (mg L^{-1}) is the concentration at equilibrium; q_{max} (mg g^{-1}) is the maximum adsorption at monolayer coverage; b (L mg $^{-1}$) is the adsorption equilibrium constant; K_F (L g^{-1}) is a Freundlich constant; n is a constant; k_{ad} (mol 2 $k\Gamma^2$) is the D-R isotherm constant; q_{ϵ} (mg g^{-1}) is the saturation capacity from D-R isotherm; ϵ is the Polanyi potential and calculated as follows:

$$\varepsilon = RT \ln (1 + 1/C_{ea})$$
 (S5)

where R (8.314 J mol $^{-1}$ K $^{-1}$) is universal gas constant; T (K) is the absolute temperature. C_{eq} (mol L $^{-1}$) is the equilibrium concentration of adsorbate.

E (kJ mol^{-1}) is the change of free energy transforming 1 mol of adsorbates from solution to the surfaces and is conducive to the estimation of adsorption reaction type, and is obtained from k_{ad} as

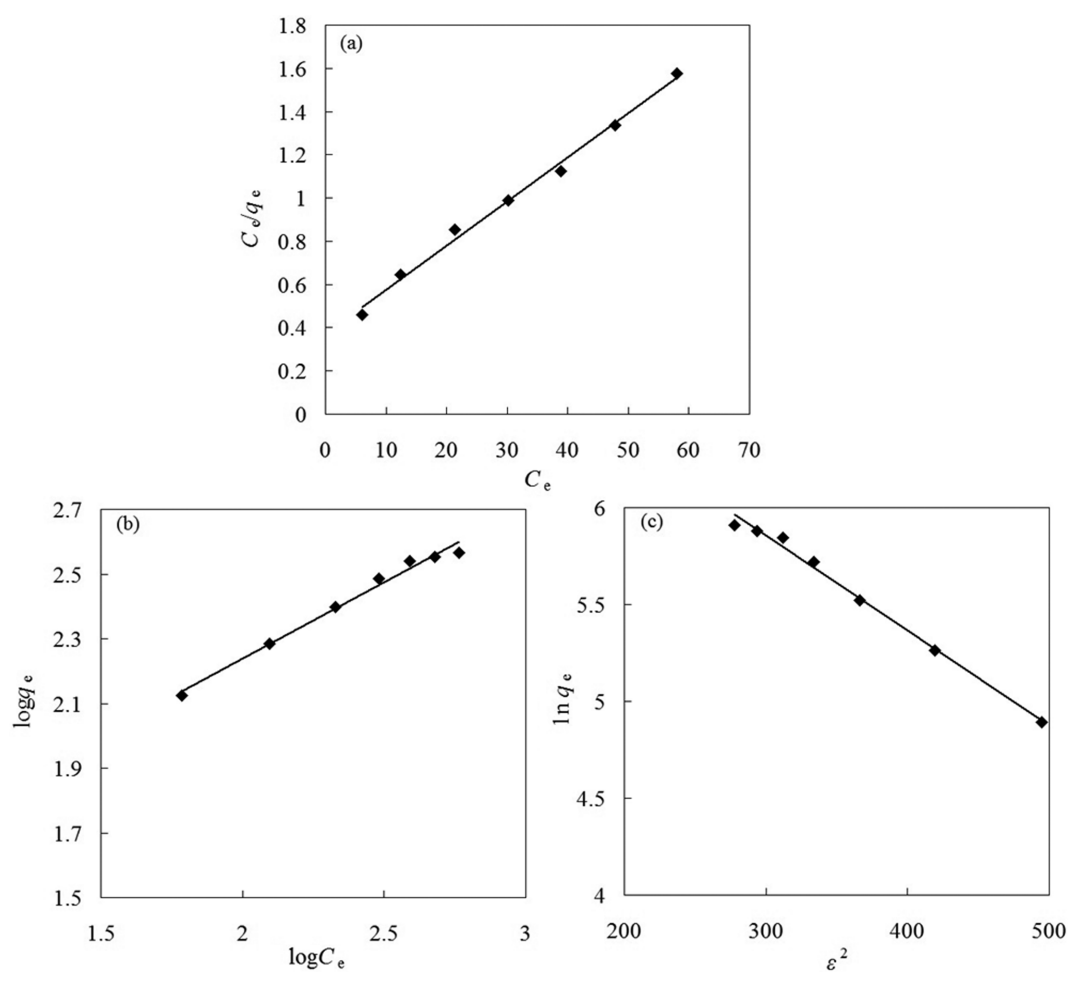


Fig. S5. Fitting plots of adsorption isotherm: (a) Langmuir, (b) Frendlich and (c) D-R.

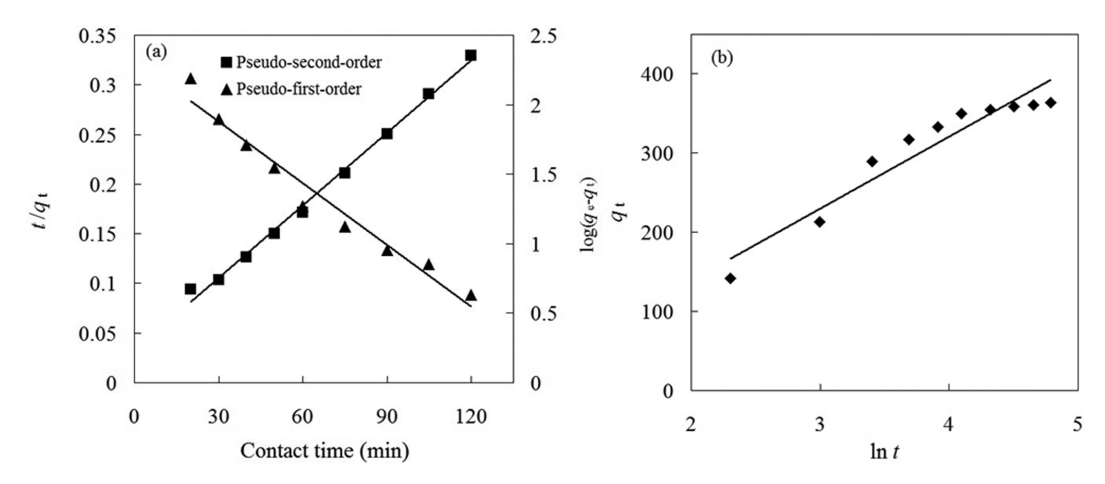


Fig. S6. Fitting plots of adsorption kinetic: (a) Pseudo-first-order, (b) pseudo-second-order and (c) Elovich equations.

follows:

$$E = -(2k_{ad})^{-1/2}$$
 (S6)

Kinetic analysis

The pseudo-first-order, pseudo-second-order and Elovich rate expressions are linearly expressed as:

$$log(q_e - q_t) = log \ q_e - k_1 t / 2.303$$
 (S7)

$$t/q_{e}=1/k_{2}q_{e}^{2}+t/q_{e}$$
 (S8)

$$q_t = (1/\beta) \ln (a\beta) + (1/\beta) \ln t$$
 (S9)

where k_1 (min⁻¹) is the rate constant of the pseudo-first-order adsorption. q_{ℓ} and q_{ℓ} (mg g^{-1}) are the adsorption capacity at equilibrium and the adsorption amount at time t (min), respectively. k_2 (g mg⁻¹ min⁻¹) is the rate constant of the pseudo-second-order equation. α is the initial adsorption rate of Elovich equation (mg·g⁻¹·min⁻¹) and β is related to the extent of surface coverage and activation energy for chemisorption.

Thermodynamic analysis

Thermodynamic parameters such as standard Gibbs free energy change (ΔG°), enthalpy change (ΔH°) and entropy change (ΔS°) at equilibrium at different temperatures can be calculated from the constant (b, L mol⁻¹) of Langmuir isotherm equation as the following equations:

$$\Delta G^o = -RT \ln b \tag{S10}$$

In order to use b in the thermodynamic calculations, the value of b expressed in L mg⁻¹ in Langmuir isotherm equation can be multiplied by 1,000 to convert the units in L g⁻¹, and then multiplied by the molecular weight of the ASA (M_r =217.06), to transform b in L mol⁻¹.

 ΔH^{o} and ΔS^{o} were obtained from Eq. (S11).

$$lnb = \frac{\Delta S^{o}}{R} - \frac{\Delta H^{o}}{RT}$$
 (S11)

CrystEngComm



PAPER

View Article Online
View Journal



Cite this: DOI: 10.1039/d3ce00693j

Improving oxygen reduction reaction and oxygen evolution reaction activities with Ru-NiCo nanoparticles decorated on porous nitrogen-doped carbon for rechargeable Zn-air batteries and OER electrocatalysts†

Lili Sui, b Lihua Miao, b *a Ye Kuang, Xiaoyan Shen, Dan Yang and He Huang *a

The slow kinetics of the oxygen evolution reaction (OER) and oxygen reduction reaction (ORR) in air cathodes severely limit the development of reversible zinc-air batteries. Thus, bifunctional oxygen catalysts with excellent electrocatalytic activity and durability for both the oxygen reduction and oxygen evolution reactions (ORR/OER) are keys to achieving long-term rechargeable zinc-air batteries. However, it remains challenging to further improve the performance by adding more active sites. To address this, a series of nitrogen-doped carbon (CN) with NiCo alloys has been synthesized by pyrolyzing a simple bimetal zeolitic-imidazolate framework (ZIF) and then evenly loaded with metallic Ru nanoparticles, resulting in Ru-NiCo/NC samples. Benefiting from the large pore volume and high activities, the Ru-NiCo/NC electrocatalysts exhibit higher ORR ($E_{1/2} = 0.84 \text{ V}$) and OER performance with an overpotential of 342 mV at 10 mA cm⁻², along with superior cycle stability. More significantly, when employed in rechargeable zinc-air batteries, Ru-NiCo/NC catalysts demonstrate a high power density of 132.3 mW cm⁻², significantly outperforming Pt and Ru-based zinc-air batteries. Additionally, DFT (density functional theory) results indicate that the addition of Ru leads to a downshift of the d-band center from the Fermi level, which benefits the reduction of energy barriers and enhances the desorption of O-containing intermediates. This work provides a feasible strategy for developing efficient and high-performance bifunctional electrocatalysts.

Received 11th July 2023, Accepted 8th September 2023

DOI: 10.1039/d3ce00693j

rsc.li/crystengcomm

1. Introduction

With the rapid development of science and technology, human beings face increasingly prominent problems, such as environmental pollution and resource shortage. The development of new fine performance and environment-friendly energy materials plays an important role in alleviating energy shortage and promoting national economic development. Among various energy storage systems, as an attractive alternative to traditional lithium-ion batteries, zinc-air batteries have higher energy density and safety, and are promising next-generation batteries. However, due to the slow kinetics of the oxygen reduction/reduction reaction

Currently, Pt based catalysts have high ORR activity, which can speed up reaction kinetics. In practice, however, cost and scarcity are major issues. Therefore, the development of low-cost, highly active alternative materials has become an urgent task. Extensive research has been carried out on transition metal oxides and nonmetallic heteroatom-doped carbon. However, the achievement of a satisfactory ORR is still a challenge. The achievement of a satisfactory of the catalytic activity of metal and nonmetal heteroatoms co-doped with carbon is similar to that of Pt-based catalysts. The mechanism is probably due to an increase in the number of active sites. These results show that transition metal heteroatom doped carbon has potential for developing efficient and low-cost ORR catalysts. However, the reported OER properties of carbon

⁽ORR/OER) and the instability of bifocal catalysts, zinc-air batteries have great energy loss and poor cycling performance. Thus, highly effective ORR catalysts are essential for energy transformation devices like fuel cells and metal-air batteries.^{7,8} In addition, the design of an efficient, affordable, and sustainable dual-function catalyst is very crucial for secondary Zn-air cells.

^a School of Medical Information Engineering, Shenyang Medical College, Shenyang 110043, Liaoning, China. E-mail: ambitious1972@163.com

b School of pharmacy, Shenyang Medical College, Shenyang, 110043, Liaoning, China

^c Shenyang Ligong University, School of Renewable Energy, Shenyang 110136, P. R. China

[†] Electronic supplementary information (ESI) available. See DOI: https://doi.org/ 10.1039/d3ce00693j

materials are usually not very good. But, the performance of ORR and OER catalysts can be effectively improved by the supported electrocatalysis strategy. Recently, transition metalbased (TM) species/carbon catalysts have attracted wide interest in Zn-air batteries on account of their moderate catalytic property for the ORR/OER. 16,17 Among various composites, zeolitic imidazolate framework (ZIF) derivatives are promising candidates for multi-functional electrocatalysts since these derivate TM-based phases/porous NC composites, which are in situ formed by the conversion of N-containing organic ligands and metal centers in ZIFs, can efficiently catalyze the reversible reactions in Zn-air cells. 18 Nevertheless, it should be noted that the significantly reduced porous channels and aggregated TMbased particles over the high-temperature calcining process will seriously deteriorate the catalytic activity of ZIF-derived catalysts especially for the OER.19 On the other hand, Ru and Ir containing materials have been proved to be superior electrocatalysts for the OER. Therefore, coating Ru or Ir on the ZIF-derived materials with enough pores and highly dispersed TM-based nanoparticles should be a highly desirable procedure to construct ideal bifunctional catalysts. In addition, transition metals are commonly used in combination with other materials, with nickel being a particularly versatile element.²⁰ NiCo alloys have been shown to exhibit superior activity and decay resistance compared to their single-metal counterparts.²¹ The bonding between different metals in these alloys can also create intrinsic polarity, thereby enhancing catalytic reactions. Moreover, nickel is known to effectively increase the graphitization degree of carbon materials. 22,23 In addition, the central metal atom is usually the ORR active site. Therefore, the selection of highly active core metal atoms is the most effective strategy to enhance catalytic activity. This is mainly due to the interaction of the d orbital of the central metal atom with the p electrons of oxygen atoms and oxygen-containing intermediates during the ORR process, which leads to the adsorption and subsequent electron transfer of oxygen molecules.²⁴ Therefore, the chemical properties of the core metal atoms will largely determine the ORR reactivity. Thus, electrocatalysts that

Herein, we designed novel Ru decorated NiCo/CN catalysts by a facile pyrolysis strategy. Due to the significantly increased Co and Ni content on the surface of the material, the large number of alloys creates favorable conditions for the formation of active sites and better spatial isolation characteristics. Then, the introduction of Ru speeds up the kinetics and improves the electrocatalytic performance of the material. Ru-NiCo/NC electrocatalysts show higher ORR ($E_{1/2}$ = 0.84 V) and OER performance with an overpotential of 342 mV at 10 mA cm⁻² and superior cycle stability. More significantly, the Ru-NiCo/NC catalysts employed in a rechargeable ZAB display a high power density of 132.3 mW cm⁻² and long cycle stability. DFT results indicate that the addition of Ru can lead to the downshift of the d-band center from the Fermi level, which could be

incorporate Ru-decorated NiCo/NC can significantly improve

the electrocatalytic performance for both the oxygen evolution

and reduction reactions (OER and ORR, respectively).

beneficial to reducing energy barriers and boosting the desorption of O-containing intermediates.

2. Results and discussion

The morphology and structural characteristics of the prepared samples were characterized by SEM and TEM. Fig. 1a shows the TEM image. It is found that the NiCo nanoparticles are encapsulated in carbon tubes. This feature was further confirmed by high resolution TEM (Fig. 1b). Simultaneously, the interplanar spacing of 0.176 nm corresponds to the (200) plane of NiCo alloys. Fig. 1c shows the microstructure of the Ru-NiCo/NC nanostructures. It's made up of a lot of curved nanotubes. The metal particles are encapsulated in the nanotubes, and there are no particles on the outside of the nanotubes. The TEM image of the Ru-NiCo/CN catalyst is shown in Fig. 1d. It consists of N-doped graphitic carbon with multilayer ultrathin nanotubes and alloy nanoparticle enrichment zones. Lines are seen around the alloy particles, indicating that the alloy is encased within. The space confinement is especially important in suppressing particle dissolution, which is beneficial for maintaining high stability in the ORR/OER process. Fig. 1(e and f) exhibit the corresponding HRTEM images. The lattice spacing of 0.179 nm can be ascribed to the (200) plane. In addition, the lattice spacing of 3.29 nm can be indexed to the (200) plane of the graphitic carbon phase. By comparing the HRTEM diagram of the two samples, it can be found that the crystal plane spacing of the prepared samples increases significantly after Ru modification. Fig. 1g presents the element distribution mappings of the Ru-NiCo/CN samples. It can be found that Ru, Co, Ni, C and N elements are uniformly distributed throughout the sample. The rich area of the alloy is mainly composed of Co, Ni and N, indicating that there may be a large number of bonds between the alloy and N.

The crystal structures of Ru-NiCo-MOF and the all samples were characterized by XRD. As shown in Fig. 2a and S1,† the characteristic diffraction peak at 26.3° can be indexed to the (002) planes of graphitic carbon. The diffraction peaks at 44.5°, 51.8° and 76.3° belong to the (111), (200), and (220) planes of Ni (JCPDS 04-0850). The other diffraction peaks can be indexed to the (111), (200), and (220) crystal planes of the Co phase (JCPDS 15-0806). The diffraction peak positions of NiCo are in agreement with the NiCo alloys obtained by Mehmood et al.25 No other diffraction peaks can be observed, indicating that the prepared sample possesses high purity and excellent crystallinity. In addition, the absence of Ru indicates that the Ru content in Ru-NiCo/NC is too low to be detected by XRD, or that they are not converted into a new phase, but are present as dopants in the catalyst. The distribution of elements and the valence states of surface elements of the prepared samples were analyzed by XPS. As shown in Fig. 2b, the Co 2p spectra of the two catalysts can be well deconvoluted into four kinds of peaks: metallic Co, Co-N, Co²⁺ and satellite peaks. The binding energies at around

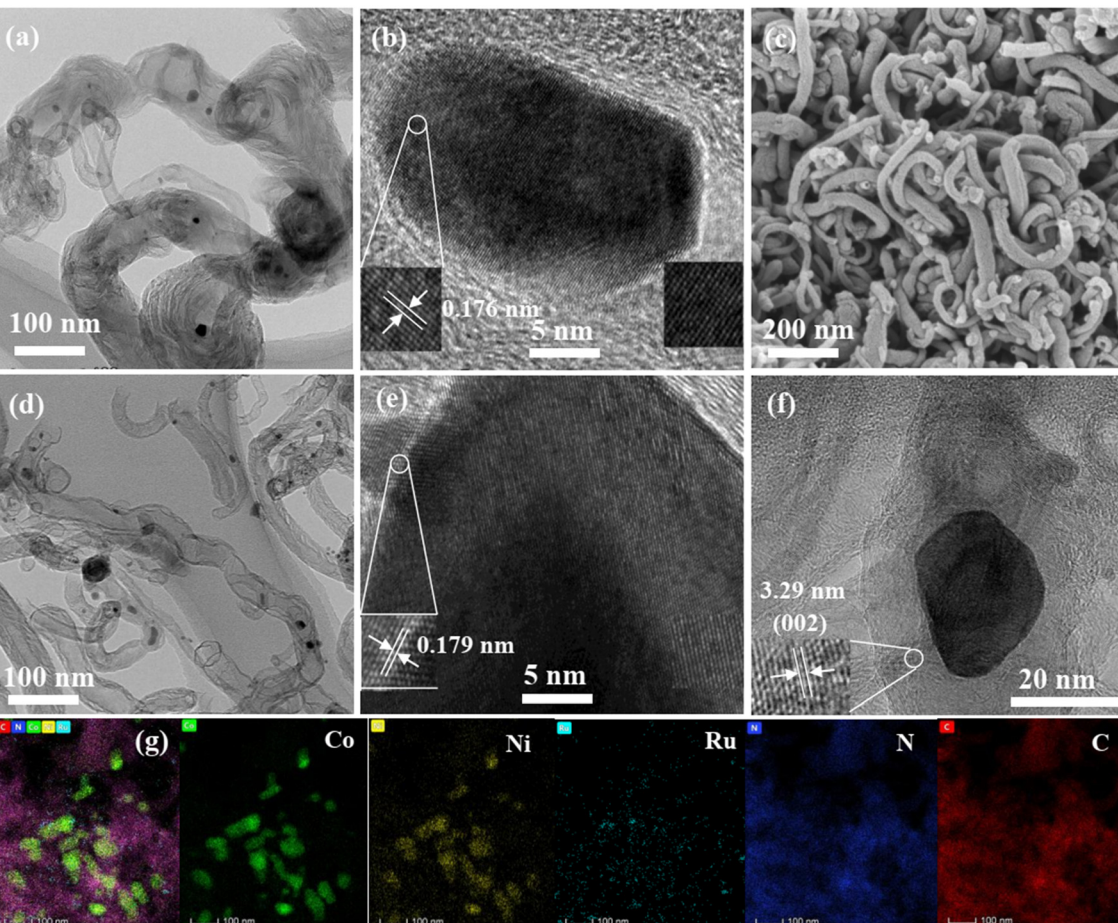


Fig. 1 (a and b) TEM and HRTEM images of NiCo/NC, (c) SEM image of the Ru-NiCo/NC catalyst. (d-f) TEM and HRTEM images of Ru-NiCo/NC. (g) Elemental mappings.

777.8 eV and 793.1 eV can be indexed to metallic Co.26 The peaks at 780.2 eV and 795.2 eV could be ascribed to Co²⁺.27 The peaks at around 782.9 eV and 798.3 eV correspond to Co-N bonds. This reveals that CoN_x possesses a high proportion, indicating that the surface of the material possesses more active sites. The binding energy of Co 2p in the samples from NiCo/NC to Ru-NiCo/NC moves to the higher energy level region, indicating the formation of strong chemical bonds. The increase of the energy level is beneficial to the enhancement of electrocatalytic performance.²⁷ The high-resolution Ni 2p spectra (Fig. 2c) show two peaks at around 852.7 and 870.0 eV, which correspond to zero-valence state metallic Ni.28 The relatively weak peaks at binding energies of 855.8 and 873.6 eV can be ascribed to Ni²⁺ 2p_{3/2} and Ni2+ 2p1/2, respectively, due to the partial oxidation of the sample exposed to air.29 In the high-resolution N 1s spectra (Fig. 2d), the four well-fitted peaks can be indexed to pyridinic-N (404.8 eV), pyrrolic-N (398.6 eV), graphitic-N (401.1 eV), and oxidized-N (401.8 eV), respectively.³⁰ The successful incorporation of nitrogen atoms into the Ru-NiCo/ NC sample leads to the modulation of the local electronic structure. This enhances the electrical conductivity and creates abundant defects/vacancies, which are favorable for

improving the electrocatalytic performance. The highresolution C 1s spectra (Fig. 2e) can be well fitted into three peaks located at 284.4, 285.3, and 289.1 eV, which are assigned to C-C, C-N, and C-O, respectively.³¹ As depicted in Fig. 2f, the deconvoluted Ru 3p peaks show binding energies at 461.6 and 483.2 eV assigned to Ru 3p_{3/2} and Ru 3p_{1/2}. ^{32,33} Fig. 2g exhibits the full spectra of the Ru-NiCo/NC and NiCo/ NC samples, confirming the existence of the Ru, Ni, Co, N and C elements. Raman spectra of the all products are measured, as shown in Fig. 2h. The peak located at 1353 cm⁻¹ can be indexed to the D band, which shows the structural defects and disorder of carbon. The Raman peak at 1591 cm⁻¹ can be ascribed to the G band, which originates from the disorder-induced C=C vibration and tangential E_{2g} sp² bonded C-C stretching vibration, respectively.³⁴ The integrated intensity ratio of the D peak to the G peak (I_D/I_G) , which represents the degree of disorder, can be calculated from the Raman spectra. The results verify that the $I_{\rm D}/I_{\rm G}$ value of Ru-NiCo/NC is 0.97, which is higher than those of Ru-Co/NC (0.94), Ru-Ni/NC (0.95), NiCo/NC (0.96), Ni/NC (0.93) and Co/NC (0.91). This suggests that the addition of the Ru element leads to an increase in the degree of graphitization. The isothermal nitrogen

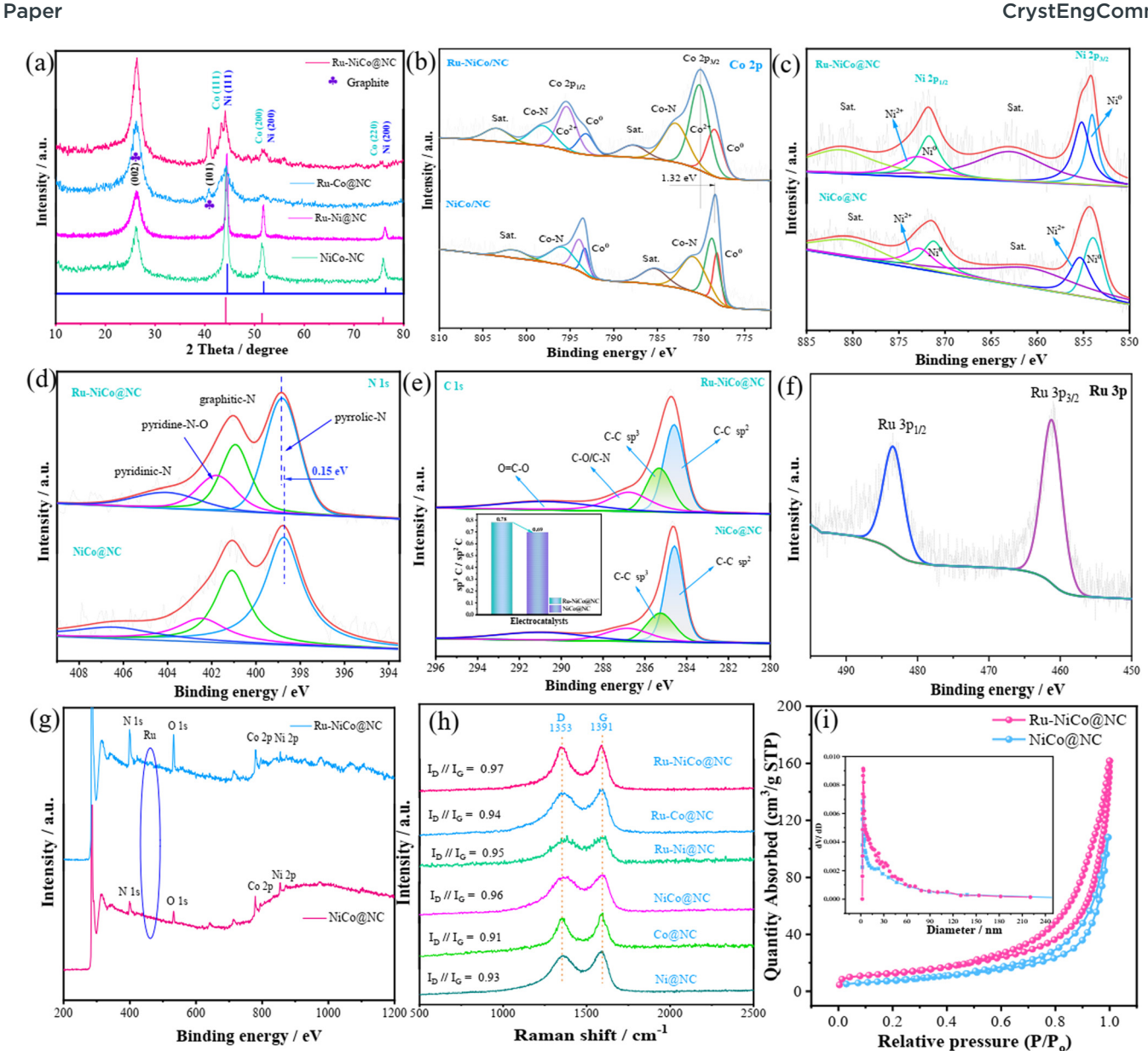


Fig. 2 (a) XRD and (b-q) XPS spectra of the as-prepared samples: (b) Co 2p, (c) Ni 2p, (d) N 1s, (e) C 1s, and (f) Ru 3p, (g) full XPS spectra, (h) Raman spectra, and (i) N₂ adsorption-desorption isotherms, the illustration shows the corresponding aperture distribution curves

desorption curves are evaluated in Fig. 2i. The IV type hysteresis loops appear in the relative pressure range of 0-1.0, indicating the existence of mesopores.³⁵ In comparison, the Ru-NiCo/NC catalyst shows a BET surface area of 84.6 m² g⁻¹, which is higher than that of NiCo/NC (58.9 m² g⁻¹). The inset shows the pore size distribution of the samples, and the Ru-NiCo/NC sample possesses a total pore volume of 18 cm³ g⁻¹. The corresponding average aperture is 2.5 nm. It is found that the Ru-NiCo/NC electrode material presents the largest pore volume and a large number of mesopores, which could lead to the increased oxygen adsorption ability and the availability of active sites.

The OER performance of the as-prepared catalysts is investigated under a three-electrode system in 1 M KOH aqueous solution. All LSV curves of the samples were obtained with IR compensation at 2 mV s⁻¹ for the OER. Fig. 3a shows the LSV curves of the as-prepared catalysts. It is found that Ru-NiCo/NC delivers a low overpotential of 342 mV at a current density of 10 mA cm⁻², which is lower than those of Ru-Co/NC (361 mV), NiCo/NC (398 mV), Co/NC (413 mV), Ru-Ni/NC (437 mV) and Ni/NC (458 mV), and the results showed that Ru modification could significantly improve the electrocatalytic performance of the materials. Meanwhile, it can be found that Co plays a major role in NiCo bimetallic electrocatalysts. The reaction kinetics of the electrocatalysts for the OER can be further analyzed from the Tafel slope, as shown in Fig. 3b. Ru-NiCo/NC exhibits the lowest Tafel slope of 65.75 mV dec⁻¹, which is smaller than those of Ru-Co/NC (65.83 mV dec⁻¹), NiCo/NC (67.99 mV dec⁻¹), Co/NC (69.78 mV dec⁻¹), Ru-Ni/NC (129.94 mV dec⁻¹)

CrystEngComm Paper

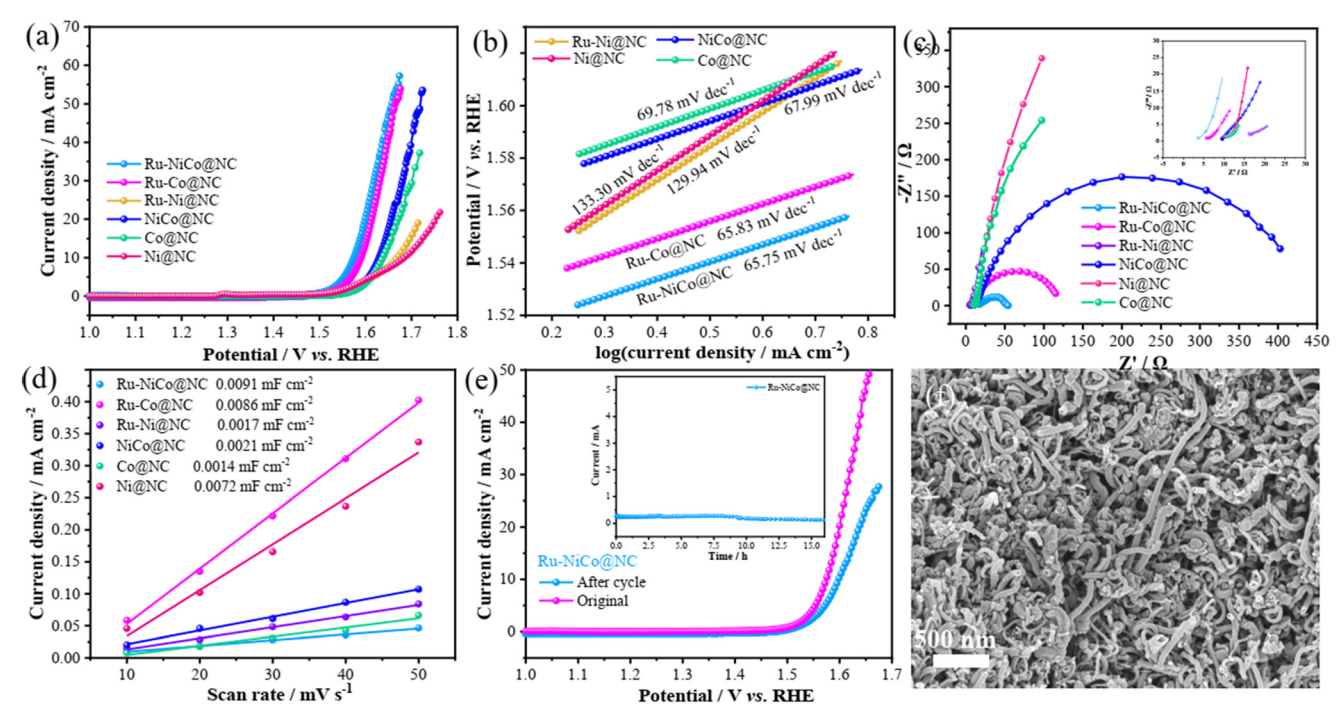


Fig. 3 Electrochemical performances of the catalysts. (a) LSV curves, (b) Tafel slopes, (c) impedance spectra, (d) double-layered capacitance linear fitting, (e) cycle stability, and (f) SEM image after cycling.

and Ni/NC (133.30 mV dec⁻¹), indicating that the Ru element decoration can effectively improve the electrocatalytic reaction kinetics. Fig. 3c shows the impedance spectra of the prepared materials. It can be seen from the inset that Ru-NiCo/NC presents a low equivalent resistance (3.7 Ω). It is confirmed that Ru-NiCo/NC has the best electrocatalytic performance compared with other materials. To further investigate the intrinsic activity of all electrocatalysts, the electrochemically active surface area (ECSA) is obtained using the electrochemical double-layer capacitance ($C_{\rm dl}$), which can be obtained through fitting the CV curve at different scan rates in the non-faradaic region, as shown in Fig. S1.† It shows that the shapes of all the curves are rectangular, meaning that they belong to the non-faradaic region. Fig. 3d shows the corresponding values of the electrochemical double-layer capacitance. The as-obtained Ru-NiCo/NC catalyst displays the largest ECSA value of 0.0091 mF cm⁻², which is higher than those of Ru-Co/NC (0.0086 mF cm⁻²), NiCo/NC $(0.0021 \text{ mF cm}^{-2})$, Co/NC $(0.0014 \text{ mF cm}^{-2})$, Ru-Ni/NC $(0.0017 \text{ mF cm}^{-2})$ and Ni/NC $(0.0072 \text{ mF cm}^{-2})$. This can be attributed to the addition of metal Ru, increasing the active sites of the electrode materials. Fig. 3e shows the cyclic stability test of the Ru-NiCo/NC electrocatalyst. It can be seen from the curve that the performance of the prepared material does not decrease significantly after cycling, which proves that it possesses many active sites and excellent structural stability. It is further confirmed from the illustration that the prepared catalyst still has good cyclic stability after 16 h. Fig. 3f shows the SEM image after cycling. Compared with the SEM image before cycling, it can be found that the material morphology is well maintained.

The ORR performance of the prepared sample was initially evaluated through CV curves. The recorded CV curves of the sample under nitrogen and oxygen conditions are shown in Fig. S2.† It can be observed that the prepared material does not exhibit any oxidation-reduction peaks when saturated with N2, while a significant reduction peak is observed for the prepared catalyst in an O2 atmosphere. This confirms that the prepared material exhibits ORR activity.36,37 The electrocatalytic performance of the prepared samples was then evaluated by LSV. As shown in Fig. 4a, the LSV curves exhibit that the Ru-NiCo/NC catalyst has the best oxygen reduction activity with a positive $E_{\rm onset}$ of 0.92 V, which is higher than those of Ru-Co/NC (0.91 V), NiCo/NC (0.90 V), Ru-Ni/NC (0.87 V), and Ni/NC (0.83 V). At the same time, Pt/C shows an $E_{\rm onset}$ of 0.95 V and half-wave potential of 0.86 V. The Ru-NiCo/CN samples present the positively shift halfwave potential (0.84 V) and a higher limiting current density (5.68 mA cm⁻²) than those of Ru-Co/NC (0.83 V@4.98 mA cm⁻²), NiCo/NC (0.82 V@3.92 mA cm⁻²), Ru-Ni/NC (0.76 $V@4.58 \text{ mA cm}^{-2}$), Ni/NC (0.80 $V@2.49 \text{ mA cm}^{-2}$). In order to further evaluate the reaction kinetics of the prepared catalyst, the corresponding Tafel slope is calculated, as presented in Fig. 4b. Ru-NiCo/NC possesses a low Tafel slope of 38.18 mV dec⁻¹, which is smaller than those of Ru-Co/NC (54.20 mV dec⁻¹), Ru-Ni/NC (38.48 mV dec⁻¹), NiCo/NC (38.4 mV dec⁻¹), Co/NC (38.4 mV dec⁻¹) and Ni/NC (60.1 mV dec⁻¹). The low Tafel slope demonstrates that Ru decoration can increase the ORR reaction kinetics. The electron transfer number of Ru-NiCo/NC was also evaluated through the LSV curves at different rotation rates ranging from 100 to 2500 rpm (Fig. 4c) according to the Koutecky–Levich (K–L) equation.³⁸

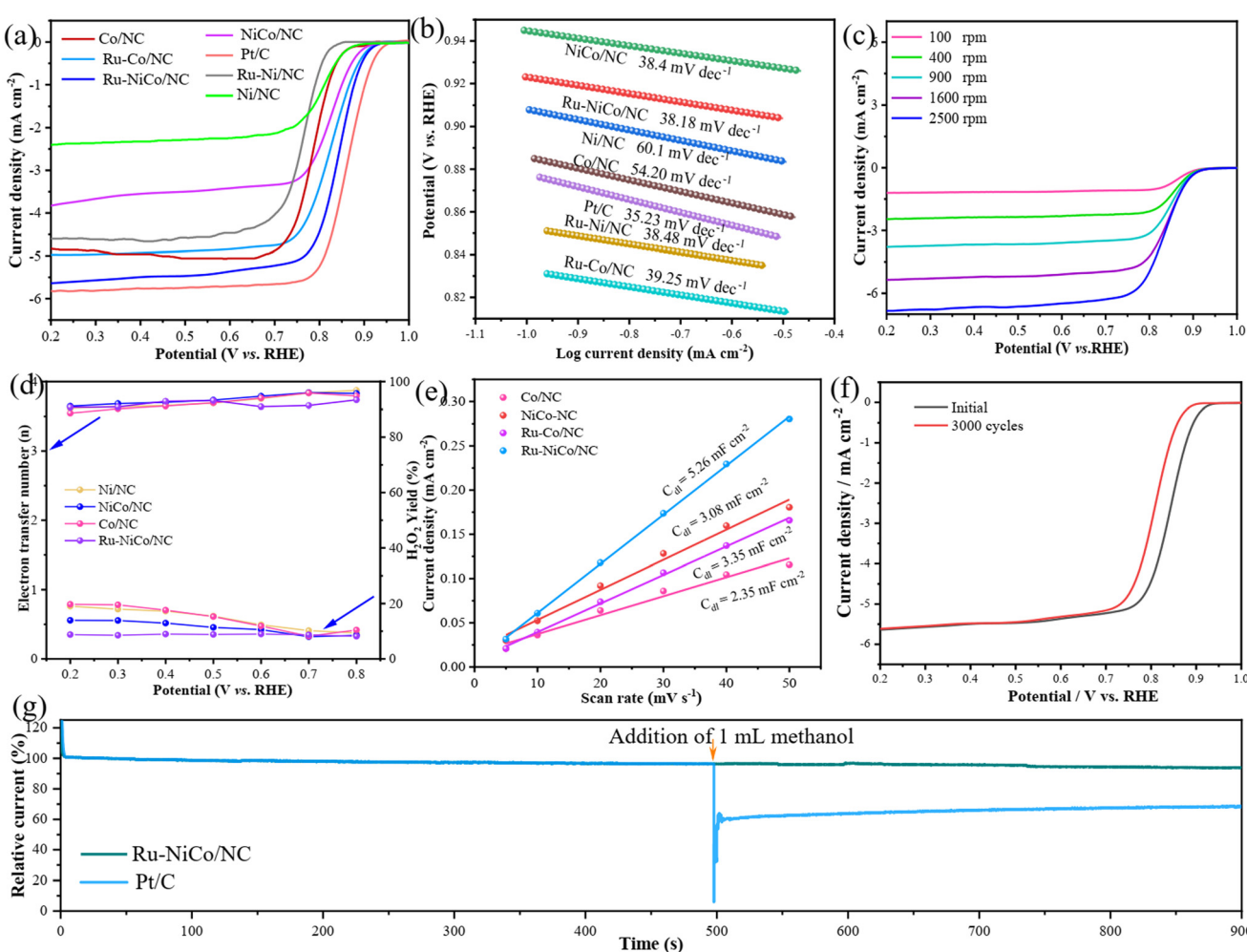


Fig. 4 Electrochemical performances of all catalysts. (a) LSV curves, (b) Tafel slopes, (c) LSV curves of the Ru–NiCo/NC sample and corresponding Koutecky–Levich plots, (d) electron-transfer number and H_2O_2 yield, (e) double-layered capacitance linear fitting, (f) LSV curves of the Ru–NiCo/NC material before and after 3000 cycles, and (g) chronoamperometric response of Ru–NiCo/NC and Pt/C upon addition of 1 mL methanol.

The n value of the as-obtained samples is 3.92. The n and H₂O₂ yield were further evaluated using a rotating ring-disk electrode (RRDE, Fig. 4d). The as-prepared material undergoes an obvious four-electron transfer process with nclose to 4 and a H₂O₂ yield of about 17%. The electrochemically active surface area (ECSA) is obtained from the double-layer capacitance, and it can be calculated from the CV curves in the non-faradaic region. In Fig. 4e, the Ru-NiCo/NC catalyst shows a high $C_{\rm dl}$ value of 5.26 mF cm⁻², which is higher than those of Ru-Co/NC (3.35 mF cm⁻²), NiCo/NC (3.08 mF cm⁻²) and Co/NC (2.35 mF cm⁻²). The results show that Ru can improve the specific activity of the electrocatalysts. Cyclic stability is an important evaluation factor, as shown in Fig. 4f. The $E_{1/2}$ of the Ru-NiCo/NC catalyst presents a low decay of 28 mV after 3000 cycles, revealing that the Ru-NiCo/NC material possesses excellent cycle stability. In addition, Ru-NiCo/NC exhibits compelling methanol tolerance after injecting methanol into the electrolyte (Fig. 4g). It is obviously superior to commercial Pt/C electrode materials.

Through the above performance test and structural characterization, it can be found that the prepared catalyst shows an excellent electrochemical performance. In order to further explore its practical application, the corresponding zinc-air battery was assembled. Zinc-air batteries have attracted wide attention owing to their high specific energy density. As shown in Fig. 5a and g, the as-obtained Ru-NiCo/ NC catalyst was used as the air cathode for the zinc-air batteries, a Zn plate was selected as the anode material and a 6.0 M KOH + 0.2 M Zn(Ac)₂ solution as the electrolyte. The assembled Ru-NiCo/NC device exhibits an open-circuit voltage of 1.44 V (Fig. 5b), which is higher than that of commercial Pt/C-RuO2. Fig. 5c presents the GCD curves of the device. The zinc-air battery with the Ru-NiCo/NC cathode catalyst delivers a peak power density of 132.3 mW cm⁻², which is higher than that of Pt/C-RuO₂ (41.2 mW cm⁻²). In addition, the zinc-air battery with the Ru-NiCo/NC cathode shows a discharge specific capacity of 767.9 mA h g⁻¹ at 10 mA cm⁻², which is higher than that of Pt/C (658.6 mA h g⁻¹) (Fig. 5e). It can be seen from Fig. 5f that the two devices can

CrystEngComm

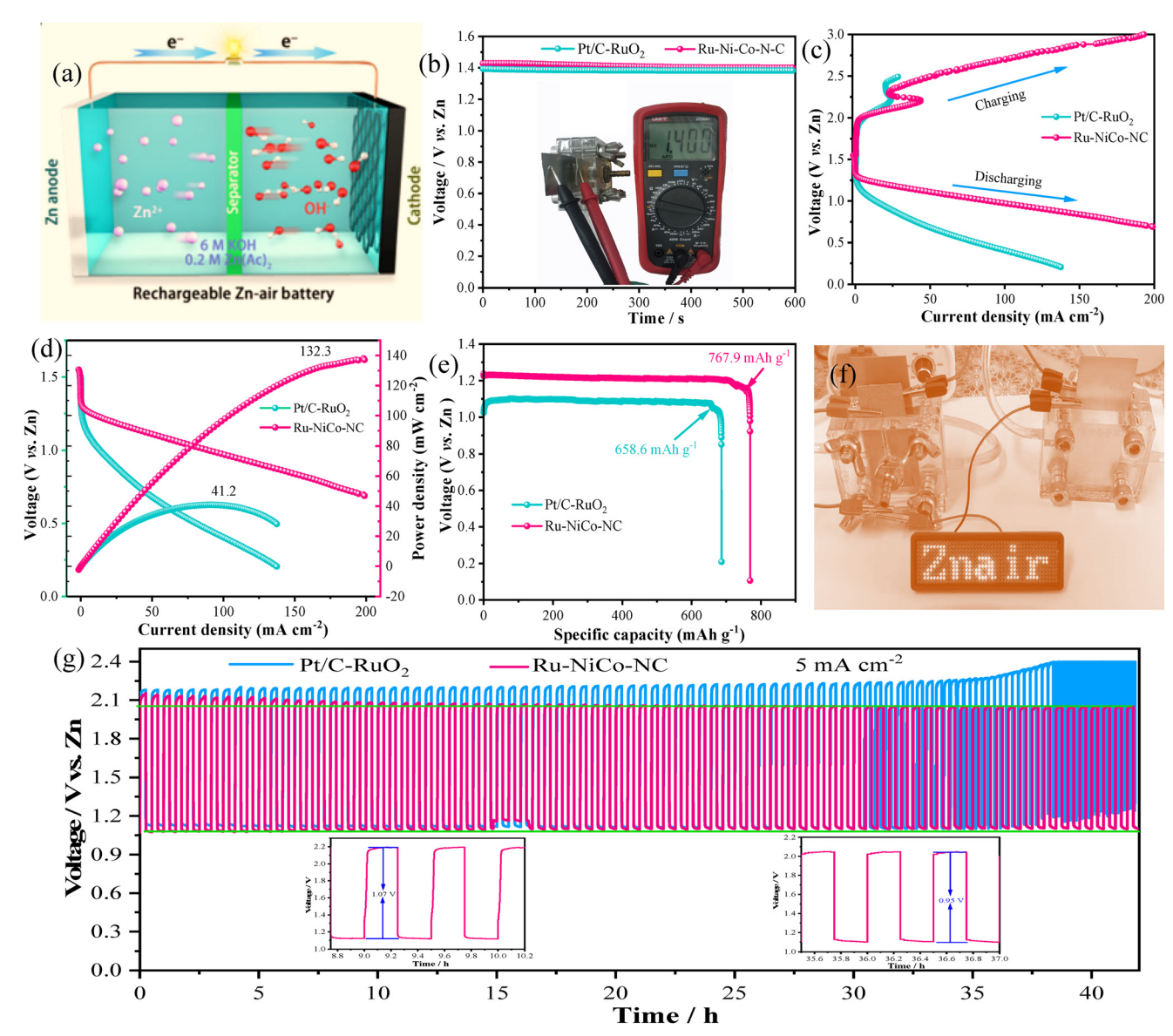


Fig. 5 (a) Schematic illustration of an aqueous ZAB, (b) digital photograph showing an open-circuit potential of 1.4 V, (c) charge and discharge polarization curves, (d) power densities, (e) specific capacities of the zinc-air battery, (f) image of the assembled device and (g) galvanostatic charge-discharge cycle curves of aqueous ZABs, inset shows the charge and discharge curves of the front and back turns.

power a display. When the zinc-air battery with the Ru-NiCo/NC cathode was galvanostatically discharged at a current density of 10 mA cm⁻² for more than 45 h, it is found that the discharge voltage is 1.07 V. The voltage decreases to 0.95 V after 45 h cycling. The results show that the prepared material exhibits excellent cycle stability (Fig. 5g and inset).

DFT calculations are employed to further understand the mechanism of Ru decoration for enhancing electrocatalytic performance. Fig. 6a and b depict the theoretical models of the NiCo/NC and Ru-NiCo/NC samples. The bonding and antibonding states of covalent bonds were characterized by the crystal orbital Hamilton population (COHP) method, as shown in Fig. 6c and d. The COHP values of Co-N and N-C bonds of the Ru-NiCo/NC material are -10.53 and -2.89, respectively, and are lower than those of the NiCo/NC product (-0.102 and -0.002). This suggests that Ru modification can improve the antibonding state near the Fermi level and that Co-N interactions are more stable and stronger than C-N bonds. Thus, the filling of antibonding states is reduced and the adsorption of H2O* is enhanced. The density of states (DOS) of the electrocatalysts is calculated and presented in Fig. 6(d and e). The analysis shows that the addition of Ru significantly increases the energy near the Fermi level, and the d band center decreases from -3.97 eV to -1.49 eV. The results show that Ru modification can significantly improve the electrical conductivity and optimize the distribution characteristics of the electronic structure. Then, we further studied the reaction energy changes caused by the introduction of Ru, as presented in Fig. 6g. By comparing the adsorption energy

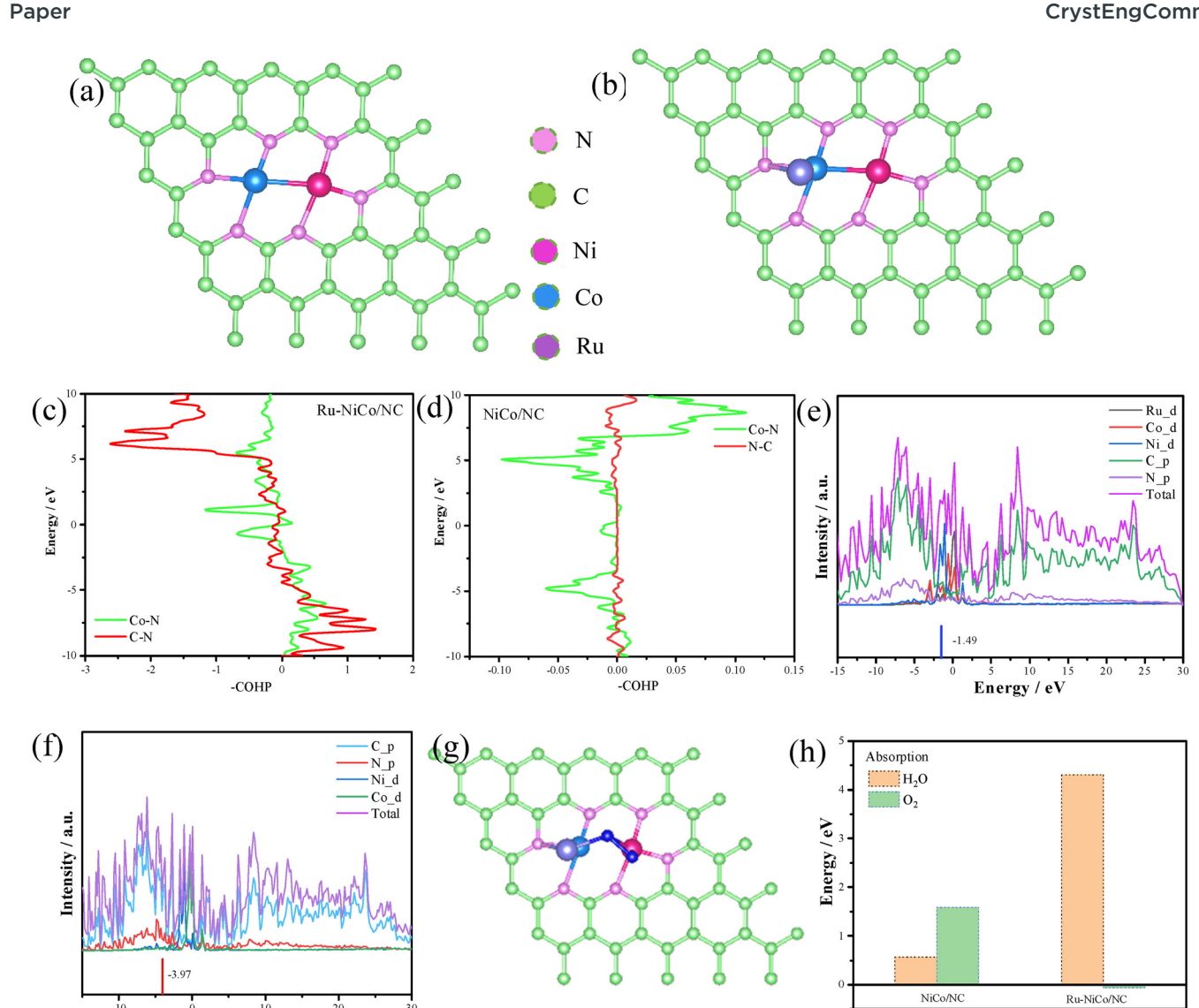


Fig. 6 Crystalline models of (a) NiCo/NC and (b) Ru-NiCo/NC, (c and d) COHP of Ru-NiCo/NC and NiCo/NC, (e) pDOS of Ru-NiCo/NC, (f) pDOS of the NiCo/NC sample, (g) model of Ru-NiCo/NC with adsorbed H₂O, and (h) adsorption energies for O₂ and H₂O.

of the Ru modified samples, it can be found that the Ru-NiCo/NC electrocatalyst exhibits strong adsorption of O₂ and H₂O, and the corresponding adsorption energies (Fig. 6h) of the Ru-NiCo/NC electrocatalyst are -0.06 eV and 4.30 eV, respectively. Its performance is better than that of the NiCo/NC electrocatalyst. The results show that the Ru-NiCo/NC electrocatalyst exhibits excellent OER and ORR performance.

Energy / eV

3. Conclusion

In summary, we designed novel Ru decorated NiCo/CN catalysts by a facile pyrolysis strategy. Due to the significantly increased Co and Ni content on the surface of the material, the large number of alloys creates favorable conditions for the formation of active sites and better spatial isolation characteristics. Meanwhile, the alloys greatly enhanced the specific surface area and degree of graphitization of the overall material. Then, the introduction of Ru speeds up the kinetics and improves the electrocatalytic performance of the material. The Ru-NiCo/NC electrocatalyst shows higher ORR ($E_{1/2} = 0.84 \text{ V}$) and OER performance with an overpotential of 342 mV at 10 mA cm⁻² and superior cycle stability. More significantly, the Ru-NiCo/NC catalyst employed in rechargeable Zn-air batteries displays a high power density of 132.3 mW cm⁻² and long cycle stability. DFT calculations show that the addition of Ru can enhance the electroactivity of the active sites. This not only increases the binding strength of the key intermediates but also reduces the overpotential of the ORR. Thus, this work provides an effective paradigm for improving catalytic kinetics and activity through noble metal modification, thereby introducing desired functionality, which may be easily extended to the design of other highly efficient catalysts.

Conflicts of interest

The authors declare no conflict of interest.

Acknowledgements

This project is supported by the Education Department of Liaoning Province (LJKMZ20221794) and the Innovative training program for college students (S202310164016).

References

- 1 T. T. Wang, W. H. Zeng, J. W. Zhu, W. X. Tian, J. Wang, J. S. Tian, D. C. Yuan, S. J. Zhang and S. C. Mu, *Nano Energy*, 2023, 113, 108577.
- 2 X. Y. Gu, M. Yu, S. Q. Chen, X. Q. Mu, Z. H. Xu, W. Q. Shao, J. J. Zhu, C. Y. Chen, S. L. Liu and S. C. Mu, *Nano Energy*, 2022, **102**, 107656.
- 3 D. Feng, P. Y. Wang, R. Qin, W. J. Shi, L. Gong, J. W. Zhu, Q. L. Ma, L. Chen, J. Yu, S. L. Liu and S. C. Mu, Adv. Sci., 2023, 10, 2300342.
- 4 F. T. Fu, Y. F. Chen, Z. M. Cui, Y. T. Li, W. D. Zhou, S. Xin, Y. W. Tang and J. B. Goodenough, *Nano Lett.*, 2016, 16, 6516–6522.
- 5 X. Luo, X. Tan, P. X. Ji, L. Chen, J. Yu and S. C. Mu, *EnergyChem*, 2023, 5, 100091.
- 6 Z. J. Li, X. D. Wu, X. Jiang, B. B. Shen, Z. S. Teng, D. M. Sun, G. T. Fu and Y. W. Tang, Adv. Powder Technol., 2022, 1, 100020.
- 7 X. Q. Mu, X. Y. Gu, S. P. Dai, J. B. Chen, Y. J. Cui, Q. Chen, M. Yu, C. Y. Chen, S. L. Liu and S. C. Mu, *Energy Environ. Sci.*, 2022, 15, 4048–4057.
- O. Keisar, Y. Ein-Eli, Y. Alfi and Y. Cohen, J. Power Sources, 2020, 450, 227545.
- 9 S. K. Singh, K. Takeyasu and J. Nakamura, *Adv. Mater.*, 2019, **31**, 1804297.
- 10 L. Zhao, Q. Wang, X. Zhang, C. Deng, Z. Li, Y. Lei and M. Zhu, ACS Appl. Mater. Interfaces, 2018, 10, 35888–35895.
- 11 J. F. Kong and W. L. Cheng, *Chin. J. Catal.*, 2017, 38, 951-969.
- 12 J. Tan, X. He, F. Yin, B. Chen, G. Li, X. Liang and H. Yin, *Catal. Today*, 2021, **364**, 67.
- 13 D. Chen, R. H. Yu, D. L. Wu, H. Y. Zhao, P. Y. Wang, J. W. Zhu, P. X. Ji, Z. H. Pu, L. Chen, J. Yu and S. C. Mu, *Nano Energy*, 2022, 100, 107445.
- 14 S. Huang, Y. Meng, Y. Cao, S. He, X. Li, S. Tong and M. Wu, *Appl. Catal.*, *B*, 2019, **248**, 239–248.
- 15 Y. Peng, Y. Bai, C. Liu, S. Cao, Q. Kong and H. Pang, *Coord. Chem. Rev.*, 2022, **466**, 214602.
- 16 L. Yang, H. Xu, H. Liu, X. Zeng, D. Cheng, Y. Huang, L. Zheng, R. Cao and D. Cao, *Research*, 2020, 9, 7593023.

- 17 P. Rao, Y. Liu, Y.-Q. Su, M. Zhong, K. Zhang, J. Luo, J. Li, C. Jia, Y. Shen, C. Shen and X. Tian, *Chem. Eng. J.*, 2021, 422, 130135
- 18 X. Wang, J. Wang, P. Wang, L. Li, X. Zhang, D. Sun, Y. Li, Y. Tang, Y. Wang and G. Fu, Adv. Mater., 2022, 34, 2206540.
- 19 H. Jiang, Y. Liu, W. Li and J. Li, Small, 2018, 14, 1703739–1703748.
- 20 X. Zhang, C. Y. Wang, Y. N. Chen, X. G. Wang, Z. J. Xie and Z. Zhou, J. Power Sources, 2018, 377, 136–141.
- 21 Y. X. Zhao, Q. X. Lai, Y. Wang, J. J. Zhu and Y. Y. Liang, ACS Appl. Mater. Interfaces, 2017, 9, 16178–16186.
- 22 B. W. Wang, X. X. Wang, J. X. Zou, Y. C. Yan, S. H. Xie, G. Z. Hu, Y. G. Li and A. G. Dong, *Nano Lett.*, 2017, 17, 2003–2009.
- 23 Z. Li, H. He, H. Cao, S. Sun, W. Diao, D. Gao, P. Lu, S. Zhang, Z. Guo, M. Li, R. Liu, D. Ren, C. Liu, Y. Zhang, Z. Yang, J. Jiang and G. Zhang, *Appl. Catal.*, B, 2019, 240, 112–121.
- 24 W. Z. Cheng, P. F. Yuan, Z. R. Lv, Y. Y. Guo, Y. Y. Qiao, X. Y. Xue, X. Liu, W. L. Bai, K. X. Wang, Q. Xu and J. N. Zhang, *Appl. Catal.*, B, 2020, 260, 118198.
- 25 A. Mukhtar, B. S. Khan and T. Mehmood, *Appl. Phys. A: Mater. Sci. Process.*, 2016, **122**, 1022.
- 26 L. Zhong, Q. Huang, J. Y. Ding, Y. Y. Guo, X. Wang, L. L. Chai, T. T. Li, Y. Hu, J. J. Qian and S. M. Huang, *J. Power Sources*, 2021, 492, 229632.
- 27 X. L. Guo, T. X. Zheng, G. P. Ji, Hu Ni, C. H. Xu and Y. X. Zhang, *J. Mater. Chem. A*, 2018, **6**, 10243–10252.
- 28 L. Yang, L. Shi, D. Wang, Y. Lv and D. Cao, *Nano Energy*, 2018, **50**, 691–698.
- 29 T. R. Zhan, X. L. Liu, S. S. Lu and W. G. Hou, *Appl. Catal.*, *B*, 2017, 205, 551–558.
- 30 W. Yao, J. M. Chen, Y. J. Wang, R. Q. Fang, Z. Qin, X. F. Yang, L. Y. Chen and Y. W. Li, Angew. Chem., Int. Ed., 2021, 60, 23729–23734.
- 31 T. H. Zhou, Y. H. Du, S. M. Yin, X. Z. Tian, H. B. Yang, X. Wang, B. Liu, H. M. Zheng, S. Z. Qiao and R. Xu, *Energy Environ. Sci.*, 2016, 9, 2563–2570.
- 32 X. Wang, Y. Jia, X. Mao, D. Liu, W. He, J. Li, J. Liu, X. Yan, J. Chen, L. Song, A. Du and X. Yao, Adv. Mater., 2020, 32, 2000966.
- 33 Y. N. Chen, X. Zhang, H. J. Cui, X. Zhang, Z. J. Xie and X. G. Wang, *Energy Storage Mater.*, 2018, **15**, 226–233.
- 34 Y. J. Huo, X. Y. Peng, X. J. Liu and J. Luo, *ACS Appl. Mater. Interfaces*, 2018, **10**, 12618–12625.
- 35 L. Xu, Q. Q. Jiang, Z. H. Xiao, X. Y. Li, J. Huo, S. Y. Wang and L. M. Dai, *Angew. Chem.*, 2016, 128, 5363–5367.
- 36 X. Li, L. Liu, X. Ren, J. Gao, Y. Huang and B. Liu, *Sci. Adv.*, 2020, **6**, eabb6833.
- 37 B. Q. Li, S. Y. Zhang, X. Chen, C. Y. Chen, Z. J. Xia and Q. Zhang, Adv. Funct. Mater., 2019, 29, 1901301.
- 38 D. J. Yang, L. J. Zhang, X. C. Yan and X. D. Yao, *Small Methods*, 2017, 1, 1700209.